1

2

Cross-neutralization of a SARS-CoV-2 antibody to

a functionally conserved site is mediated by avidity

5

6   Hejun Liu[1,*], Nicholas C. Wu[1,*], Meng Yuan[1,*], Sandhya Bangaru[1], Jonathan L. Torres[1],

7   Tom G. Caniels[2], Jelle van Schooten[2], Xueyong Zhu[1], Chang-Chun D. Lee[1], Philip J.M.

8   Brouwer[2], Marit J. van Gils[2], Rogier W. Sanders[2,3], Andrew B. Ward[1,4,5], Ian A.

9   Wilson[1,4,5,6,§]

10

11

12   [1] Department of Integrative Structural and Computational Biology, The Scripps Research

13   Institute, La Jolla, CA 92037, USA

14   [2] Department of Medical Microbiology, Amsterdam UMC, University of Amsterdam

15   [3] Department of Microbiology and Immunology, Weill Medical College of Cornell

16   University, New York, NY 10021, USA

17   [4] IAVI Neutralizing Antibody Center, The Scripps Research Institute, La Jolla, CA 92037,

18   USA

19   [5] Consortium for HIV/AIDS Vaccine Development (CHAVD), The Scripps Research

20   Institute, La Jolla, CA 92037, USA

21   [6] The Skaggs Institute for Chemical Biology, The Scripps Research Institute, La Jolla,

22   CA, 92037, USA

23   * These authors contributed equally to this work

24   § Correspondence: wilson@scripps.edu (I.A.W.)
25

1

26 **ABSTRACT**

27 Most antibodies isolated from COVID-19 patients are specific to SARS-CoV-2. COVA1-

28 16 is a relatively rare antibody that also cross-neutralizes SARS-CoV. Here we determined

29 a crystal structure of COVA1-16 Fab with the SARS-CoV-2 RBD, and a negative-stain EM

30 reconstruction with the spike glycoprotein trimer, to elucidate the structural basis of its

31 cross-reactivity. COVA1-16 binds a highly conserved epitope on the SARS-CoV-2 RBD,

32 mainly through a long CDR H3, and competes with ACE2 binding due to steric hindrance

33 rather than epitope overlap. COVA1-16 binds to a flexible up conformation of the RBD on

34 the spike and relies on antibody avidity for neutralization. These findings, along with

35 structural and functional rationale for the epitope conservation, provide a blueprint for

36 development of more universal SARS-like coronavirus vaccines and therapies.

37

MAIN

The ongoing coronavirus infectious disease 2019 (COVID-19) pandemic of severe acute respiratory syndrome coronavirus 2 (SARS-CoV-2) [1] is unlikely to end anytime soon [2]. Given the current lack of protective vaccines and antivirals, virus clearance and recovery of SARS-CoV-2 patients have to rely mainly on the generation of a neutralizing antibody response. To date, most neutralizing antibodies from convalescent patients target the receptor-binding domain (RBD) on the trimeric spike (S) glycoprotein [3-7], whose natural function is to mediate viral entry by first attaching to the human receptor angiotensin-converting enzyme 2 (ACE2) and then fusing its viral membrane with the host cell [1, 8-11]. SARS-CoV-2 is phylogenetically closely related to SARS-CoV [1], which caused the 2002-2003 human epidemic. However, SARS-CoV-2 and SARS-CoV only share 73% amino-acid sequence identity in their RBD, compared to 90% in their S2 fusion domain. Nevertheless, a highly conserved epitope on the SARS-CoV-2 RBD was previously identified from studies of a SARS-CoV neutralizing antibody CR3022 [12, 13], which was originally isolated almost 15 years ago [14]. Many human monoclonal antibodies have now been shown to target the SARS-CoV-2 S protein [3-7, 13, 15-24], but cross-neutralizing antibodies are relatively uncommon in COVID-19 patients [5, 6, 19, 25]. To date, the only structurally characterized cross-neutralizing human antibodies are S309 [18] and ADI-56046 [17] from SARS-CoV survivors, as well as EY6A from a COVID-19 patient [26]. Such structural and molecular characterization of cross-neutralizing antibodies is extremely valuable for therapeutic and vaccine design to confer broader protection against human SARS-like viruses that include the extensive reservoir of zoonotic coronaviruses in bats, camels, pangolins etc.

Antibody COVA1-16 was recently isolated from a convalescent COVID-19 patient and can cross-neutralize both SARS-CoV-2 (IC_{50} 0.13 μg/mL) and SARS-CoV (IC_{50} 2.5 μg/mL)

3

64   pseudovirus [6]. The heavy and light chains of COVA1-16 are encoded by IGHV1-46,

65   IGHD3-22, IGHJ1, and by IGKV1-33, IGKJ4, with a relatively long complementarity

66   determining region (CDR) H3 of 20 amino acids (Figure S1). IGHV of COVA1-16 is only

67   1% somatically mutated at the nucleotide sequence level (one amino-acid change) from

68   the germline gene, whereas its IGKV is 1.4% somatically mutated (three amino-acid

69   changes). Here we determined the crystal structure of COVA1-16 in complex with SARS-

70   CoV-2 RBD at 2.89 Å resolution to identify its binding site (epitope) and mechanism of

71   cross-neutralization (Figure 1A, Table S1). The epitope of COVA1-16 overlaps extensively

72   with that of CR3022, but also extends towards the periphery of the ACE2 binding site

73   (Figure 1B) [13]. Seventeen out of 25 residues in the COVA1-16 epitope overlap with the

74   CR3022 binding site (17 of 28 residues) (Figure 1C). Consistent with structural

75   identification of its epitope, COVA1-16 can compete with CR3022 for RBD binding (Figure

76   S2). COVA1-16 appears to have some resemblance to SARS-CoV cross-neutralizing

77   antibody ADI-56046, whose epitope appears to span both the CR3022 epitope and ACE2-

78   binding site, as indicated by negative-stain electron microscopy (nsEM) [17]. Interestingly,

79   COVA1-16 also competes with ACE2 for RBD binding (Figure S2) [6], although its epitope

80   does not overlap the ACE2 binding site (Figure 1B). Therefore, COVA1-16 inhibits ACE2

81   binding due to steric hindrance with its light chain rather than by direct interaction with the

82   receptor binding site (Figure 1D).

83

84   The RBD can adopt up and down conformations on the S trimer [27, 28]. While the ACE2

85   receptor only binds the RBD in the up conformation [9], previously characterized cross-

86   neutralizing antibodies S309 from a convalescent SARS-CoV patient and COVA2-15 from

87   a SARS-CoV-2 patient [6], can bind the RBD in both up and down conformations [18, 27].

88   However, unlike S309, the COVA1-16 epitope is completely buried when the RBD is in

89   the down conformation (Figure 2A), akin to the CR3022 epitope [13]. Even in the up

4

90   conformation of the RBD on an unliganded SARS-CoV-2 S trimer [27], the epitope of

91   COVA1-16 would not be fully exposed (Figure 2A). We thus performed nsEM analysis of

92   COVA1-16 in complex with the SARS-CoV-2 S trimer (Figure 2B). Three-dimensional (3D)

93   reconstructions revealed that COVA1-16 can bind to a range of RBD orientations on the

94   S protein when in the up position, indicating its rotational flexibility (Figure 2C). COVA1-

95   16 can bind the S trimer either from the top (i.e. perpendicular to the trimer apex, Figure

96   2C, yellow, blue and pink) or from the side (i.e. more tilted, Figure 2C, brown). Model fitting

97   of the COVA1-19/RBD crystal structure into the nsEM map indicates that the RBD on the

98   S trimer is more open around the apex when COVA1-16 binds compared to unliganded

99   trimers (Figure S3A-B). Bivalent binding of the COVA1-16 IgG between adjacent S trimers

100   also appears to be plausible (Figure S3C). A recent cryo-electron tomography (cryo-ET)

101   analysis demonstrated that the average distance between prefusion S on the viral surface

102   is around 150 Å [29], which is comparable to the distance spanned between the tip of the

103   two Fabs on an IgG (typically around 100 Å to 150 Å, although longer distances have been

104   observed) [30]. Indeed, COVA1-16 IgG binds much more tightly than Fab to SARS-CoV-

105   2 RBD, with dissociation constants (K_D) of 0.2 nM and 46 nM, respectively (Figure S4A),

106   reflecting bivalent binding in the assay format. Similarly, COVA1-16 IgG binds more

107   strongly than Fab to SARS-CoV RBD (K_D of 125 nM vs 405 nM) (Figure S4B). Moreover,

108   the apparent affinity of COVA1-16 IgG decreased to approximately the Fab value when

109   the amount of SARS-CoV-2 RBD loaded on the biosensor was decreased, substantiating

110   the notion that COVA1-16 can bind bivalently in this assay (Figure S4C).

111

112   Bivalent IgG binding is also important for the neutralization activity of COVA1-16 (Figure

113   2D-E). COVA1-16 IgG neutralizes SARS-CoV-2 pseudovirus with a half maximal inhibitory

114   concentration (IC_{50}) of 0.02 µg/mL, which is similar to that previously measured for SARS-

115   CoV-2 pseudovirus (IC_{50} of 0.13 µg/mL) [6]. In contrast, COVA1-16 Fab does not

116   neutralize SARS-CoV-2 pseudovirus even up to 13 µg/mL. A similar effect is also

117   observed for SARS-CoV pseudovirus, which is neutralized by COVA1-16 IgG at an IC_{50}

118   of 29 µg/mL, but not by COVA1-16 Fab even up to 67 µg/mL (Figure 2E). Of note, COVA1-

119   16 is less potent against authentic SARS-CoV-2 (IC_{50} = 0.75 µg/mL) [6]. Whether such a

120   difference is due to variation in S protein density on the viral surface versus pseudovirus

121   or to other factors deserves future investigation. It will also be informative to compare the

122   number, density and conformational states of the S proteins on SARS-CoV-2 and SARS-

123   CoV virions. Overall, our findings support the importance of bivalent binding for SARS-

124   CoV-2 neutralizing antibodies, and especially for cross-neutralization of SARS-CoV. Such

125   a contribution of bivalent IgG (avidity) to SARS-CoV-2 neutralization has also been

126   suggested in a recent study that compared binding of polyclonal IgGs and Fabs [24].

127   Furthermore, a single-domain camelid antibody VHH-72 dramatically improved its

128   neutralization activity to SARS-CoV-2 when expressed as a bivalent Fc-fusion [31]. These

129   observations are similar to some influenza broadly neutralizing antibodies to the

130   hemagglutinin (HA) receptor binding site, where bivalent binding can increase avidity and

131   neutralization breadth [32, 33].

132

133   Next we examined the molecular details of the interactions between COVA1-16 and

134   SARS-CoV-2. COVA1-16 binding to the RBD is dominated by the heavy chain, which

135   accounts for 82% of its total buried surface area (BSA, 694 $Å^2$ out of a total of 844 $Å^2$).

136   Most of the interactions are mediated by CDR H3 (Figure 3A), which contributes 70% (594

137    $Å^2$) of the total BSA. CDR H3 forms a beta-hairpin with a type I beta-turn at its tip and is

138   largely encoded by IGHD3-22 (from V_H N98 to V_H Y100f, Figure S1C and Figure 3B). The

139   beta-hairpin conformation is stabilized by four main chain-main chain hydrogen-bonds (H-

140   bonds) and a side chain-side chain H-bond between V_H N98 and V_H Y100f at either end

141   of the IGHD3-22-encoded region (Figure 3B). Four H-bonds between the tip of CDR H3

6

142 and the RBD are formed from two main chain-main chain interactions with RBD C379,

143 and two with V_H R100b (Table S2). The positively charged guanidinium of V_H R100b also

144 interacts with the negative dipole at the C-terminus of a short α-helix in the RBD (residues

145 Y365 to Y369). Interestingly, V_H R100b is a somatically mutated residue (codon = AGG in

146 the IGHD3-22-encoded region, where the germline residue is a Ser (codon = AGT, Figure

147 S1C). The short Ser side chain would likely not contact the RBD nor provide electrostatic

148 complementarity. Interestingly, a somatic revertant V_H R100bS actually improved binding

149 affinity of COVA1-16 to the RBD, mostly due to an increased on-rate (Figure S5).

150 Nevertheless, COVA1-16 has a much slower off-rate than its V_H R100bS mutant, which

151 may have led to its selection. The CDR H3 tip also interacts with the RBD through

152 hydrophobic interactions between V_H Y99 and the aliphatic portion of RBD K378, as well

153 as a π−π interaction between V_H Y100 and the RBD V382-S383 peptide backbone (Figure

154 3B). CDR H3 forms an additional four H-bonds with the RBD, involving the side chains of

155 V_H R97 and Q101 (Figure 3B). We further determined the unliganded structure of COVA1-

156 16 Fab to 2.53 Å resolution and found that the CDR H3 distal region was not resolved due

157 to lack of electron density indicating its inherent flexibility (Figure S6). CDR H1 and CDR

158 L2 of COVA1-16 also interact with the RBD, but much less so compared to CDR H3. The

159 V_H T28 main chain and V_H Y32 side chain in CDR H1 H-bond with D427 (Figure 3C, Table

160 S2), whereas V_L N53 in CDR L2 H-bonds with RBD R408 (Figure 3D, Table S2).

161

162 CDR H3-dominant antibodies have been seen in the human immune response to other

163 viral pathogens. Striking examples are antibodies PG9 and PG16, whose CDR H3s

164 interact extensively along their length with the apex of the HIV-1 Envelope protein [34, 35].

165 Another example is C05, which is essentially a single loop binder that inserts its very long

166 CDR H3 (24 residues) into the RBD of influenza HA [32], thereby providing a template for

167 design of a high-avidity protein inhibitor of influenza virus, where the H3 loop was fused

168   to a scaffold protein [36]. The long CDR H3 of COVA1-16 may similarly facilitate

169   therapeutic designs that could also include peptide-based antivirals, as exemplified by a

170   potent cyclic peptide fusion inhibitor of influenza HA [37, 38].

171

172   Compared to the ACE2-binding site, the COVA1-16 epitope is much more highly

173   conserved among SARS-CoV-2, SARS-CoV, and other SARS-related coronaviruses

174   (SARSr-CoV) (Figure 4A-D, Figure S7 and Figure S8) [6]. To investigate possible

175   structural and functional reasons for this sequence conservation, we analyzed the epitope

176   location in the context of the SARS-CoV-2 trimeric S protein with all RBDs in the "down"

177   conformation [39] (Figure 4E and Figure S7). The COVA1-16 epitope is completely buried

178   at the center of the trimer in the interface between the S1 and S2 domains and is largely

179   hydrophilic (Figure S9). The polar side chains of K378, Q414, R408, and D427, which are

180   involved in binding to COVA1-16, are all very close to the interface with adjacent

181   protomers in the S trimer. Interestingly, the R408 side chain, which is positioned by Q414

182   via a H-bond, points towards a region in the adjacent protomer 2 with a positive

183   electrostatic potential. Similarly, D427 is juxtaposed to a region in protomer 2 with a

184   negative electrostatic potential. These repulsive charges would help favor the metastability

185   required for transient opening and closing of the RBD in "up" and "down" conformations

186   prior to ACE2 receptor binding. In contrast, the K378 side chain points towards a region

187   in protomer 3 with negative electrostatic potential, thus favoring the "down" RBD

188   conformation. Furthermore, in the "down" conformation, part of the COVA1-16 epitope

189   interacts with the long helices formed from the heptad repeat motifs of S2 fusion domain

190   (Figure 4E-F). Notably, S383 and T385 in the COVA1-16 epitope make three H-bonds

191   with the tops of the helices and their connecting regions (Figure 4F). This mixture of

192   attractive and repulsive forces would seem to be important for control of the dynamics of

193   the RBD and, hence, for the biological function of the metastable pre-fusion S protein in

194   receptor binding and fusion. The complementarity of fit of the epitope interface with the

195   other RBDs and the S2 domain in the S trimer further explains the epitope conservation

196   (Figure S10). Therefore, the high sequence conservation of the COVA1-16 epitope

197   appears related to the functional requirement for this component of the RBD surface to be

198   deeply buried within the S trimer in the "down" conformation.

199

200   From the SARS-CoV-2 RBD/antibody complex structures to date, a significant portion of

201   the RBD surface can be targeted by antibodies (Figure 5). One surface not yet observed

202   to be targeted is partially covered by N-glycans at residues N165 on the N-terminal domain

203   (NTD) and N343 on the RBD, which may hinder B cell receptor access and create a "silent

204   face" (Figure S11), although the N343 glycan is incorporated in the S309 epitope [18].

205   While antibodies that target the ACE2-binding site, such as BD23 [7], CB6 [23], B38 [20],

206   P2B-2F6 [19], CC12.1 [40], and CC12.3 [40], do not show cross-neutralization activity to

207   SARS-CoV, the conserved epitopes further from the ACE2-binding site seem to be more

208   able to support cross-neutralization [13, 18, 26]. It is also interesting that these so far rare

209   cross-neutralizing antibodies, including COVA1-16, often seem to bind to epitopes that

210   are not readily accessible in the pre-fusion native structure [17, 26]. This finding is similar

211   to a recent discovery in influenza virus, where a class of cross-protective antibodies target

212   a conserved epitope in the trimeric interface of the HA [41-43]. Due to the inaccessibility

213   of the COVA1-16 epitope on the S protein, it is possible that an RBD-based rather than S-

214   based immunogen can elicit larger numbers of COVA1-16-like antibodies. Cross-

215   neutralizing antibodies have also provided important insights into therapeutic and vaccine

216   design, as for influenza virus [44] and HIV [45]. As SARS-CoV-2 continues to circulate in

217   the human population and other zoonotic coronaviruses constitute future pandemic

218   threats [46], it is certainly worth considering the development of more universal

219   coronavirus vaccines and therapeutics that can cross-neutralize antigenically drifted

220   SARS-CoV-2 viruses, as well as zoonotic SARS-like coronaviruses.

221

222   **REFERENCES**

223   1.   Zhou P, Yang XL, Wang XG, Hu B, Zhang L, Zhang W, et al. A pneumonia
224   outbreak associated with a new coronavirus of probable bat origin. Nature.
225   2020;579:270-3. Epub 2020/02/06. doi: 10.1038/s41586-020-2012-7. PubMed
226   PMID: 32015507.

227   2.   Kissler SM, Tedijanto C, Goldstein E, Grad YH, Lipsitch M. Projecting the
228   transmission dynamics of SARS-CoV-2 through the postpandemic period.
229   Science. 2020;368:860-8. Epub 2020/04/16. doi: 10.1126/science.abb5793.
230   PubMed PMID: 32291278; PubMed Central PMCID: PMCPMC7164482.

231   3.   Zost SJ, Gilchuk P, Chen RE, Case JB, Reidy JX, Trivette A, et al. Rapid
232   isolation and profiling of a diverse panel of human monoclonal antibodies
233   targeting the SARS-CoV-2 spike protein. Nat Med. 2020. doi:
234   10.1101/2020.05.12.091462.

235   4.   Robbiani DF, Gaebler C, Muecksch F, Lorenzi JCC, Wang Z, Cho A, et al.
236   Convergent antibody responses to SARS-CoV-2 in convalescent individuals.
237   Nature. 2020. doi: 10.1038/s41586-020-2456-9.

238   5.   Rogers TF, Zhao F, Huang D, Beutler N, Burns A, He W-t, et al. Isolation of
239   potent SARS-CoV-2 neutralizing antibodies and protection from disease in a
240   small animal model. Science. 2020. doi: 10.1126/science.abc7520.

241   6.   Brouwer PJM, Caniels TG, van der Straten K, Snitselaar JL, Aldon Y, Bangaru S,
242   et al. Potent neutralizing antibodies from COVID-19 patients define multiple
243   targets of vulnerability. Science. 2020. doi: 10.1126/science.abc5902.

244   7.   Cao Y, Su B, Guo X, Sun W, Deng Y, Bao L, et al. Potent neutralizing antibodies
245   against SARS-CoV-2 identified by high-throughput single-cell sequencing of
246   convalescent patients' B cells. Cell. 2020;182:73-84. Epub 2020/05/20. doi:
247   10.1016/j.cell.2020.05.025. PubMed PMID: 32425270; PubMed Central PMCID:
248   PMCPMC7231725.

249   8.   Letko M, Marzi A, Munster V. Functional assessment of cell entry and receptor
250   usage for SARS-CoV-2 and other lineage B betacoronaviruses. Nat Microbiol.
251   2020;5:562-9. Epub 2020/02/26. doi: 10.1038/s41564-020-0688-y. PubMed
252   PMID: 32094589.

253   9.   Yan R, Zhang Y, Li Y, Xia L, Guo Y, Zhou Q. Structural basis for the recognition
254   of the SARS-CoV-2 by full-length human ACE2. Science. 2020;367:1444-8. Epub
255   2020/03/07. doi: 10.1126/science.abb2762. PubMed PMID: 32132184.

256   10.   Lan J, Ge J, Yu J, Shan S, Zhou H, Fan S, et al. Structure of the SARS-CoV-2
257   spike receptor-binding domain bound to the ACE2 receptor. Nature.

258   2020;581(7807):215-20. Epub 2020/04/01. doi: 10.1038/s41586-020-2180-5.
259   PubMed PMID: 32225176.

260   11.   Shang J, Wan Y, Luo C, Ye G, Geng Q, Auerbach A, et al. Cell entry
261   mechanisms of SARS-CoV-2. Proc Natl Acad Sci U S A. 2020;117(21):11727-34.
262   Epub 2020/05/08. doi: 10.1073/pnas.2003138117. PubMed PMID: 32376634;
263   PubMed Central PMCID: PMCPMC7260975.

264   12.   Tian X, Li C, Huang A, Xia S, Lu S, Shi Z, et al. Potent binding of 2019 novel
265   coronavirus spike protein by a SARS coronavirus-specific human monoclonal
266   antibody. Emerg Microbes Infect. 2020;9(1):382-5. Epub 2020/02/18. doi:
267   10.1080/22221751.2020.1729069. PubMed PMID: 32065055.

268   13.   Yuan M, Wu NC, Zhu X, Lee CD, So RTY, Lv H, et al. A highly conserved cryptic
269   epitope in the receptor-binding domains of SARS-CoV-2 and SARS-CoV.
270   Science. 2020;368(6491):630-3. Epub 2020/04/05. doi:
271   10.1126/science.abb7269. PubMed PMID: 32245784.

272   14.   ter Meulen J, van den Brink EN, Poon LL, Marissen WE, Leung CS, Cox F, et al.
273   Human monoclonal antibody combination against SARS coronavirus: synergy
274   and coverage of escape mutants. PLoS Med. 2006;3(7):e237. Epub 2006/06/27.
275   doi: 10.1371/journal.pmed.0030237. PubMed PMID: 16796401; PubMed Central
276   PMCID: PMCPMC1483912.

277   15.   Li W, Drelich A, Martinez DR, Gralinski L, Chen C, Sun Z, et al. Potent
278   neutralization of SARS-CoV-2 in vitro and in an animal model by a human
279   monoclonal antibody. bioRxiv. 2020. doi: 10.1101/2020.05.13.093088.

280   16.   Andreano E, Nicastri E, Paciello I, Pileri P, Manganaro N, Piccini G, et al.
281   Identification of neutralizing human monoclonal antibodies from Italian Covid-19
282   convalescent patients. bioRxiv. 2020. doi: 10.1101/2020.05.05.078154.

283   17.   Wec AZ, Wrapp D, Herbert AS, Maurer D, Haslwanter D, Sakharkar M, et al.
284   Broad neutralization of SARS-related viruses by human monoclonal antibodies.
285   Science. 2020. doi: 10.1126/science.abc7424.

286   18.   Pinto D, Park YJ, Beltramello M, Walls AC, Tortorici MA, Bianchi S, et al. Cross-
287   neutralization of SARS-CoV-2 by a human monoclonal SARS-CoV antibody.
288   Nature. 2020. Epub 2020/05/19. doi: 10.1038/s41586-020-2349-y. PubMed
289   PMID: 32422645.

290   19.   Ju B, Zhang Q, Ge J, Wang R, Sun J, Ge X, et al. Human neutralizing antibodies
291   elicited by SARS-CoV-2 infection. Nature. 2020. Epub 2020/05/27. doi:
292   10.1038/s41586-020-2380-z. PubMed PMID: 32454513.

293   20.   Wu Y, Wang F, Shen C, Peng W, Li D, Zhao C, et al. A noncompeting pair of
294   human neutralizing antibodies block COVID-19 virus binding to its receptor
295   ACE2. Science. 2020;368:1274-8. Epub 2020/05/15. doi:
296   10.1126/science.abc2241. PubMed PMID: 32404477; PubMed Central PMCID:
297   PMCPMC7223722.

298   21.   Chi X, Yan R, Zhang J, Zhang G, Zhang Y, Hao M, et al. A neutralizing human
299   antibody binds to the N-terminal domain of the Spike protein of SARS-CoV-2.
300   Science. 2020;368:1274-8. doi: 10.1126/science.abc6952.

301   22.   Seydoux E, Homad LJ, MacCamy AJ, Parks KR, Hurlburt NK, Jennewein MF, et
302   al. Analysis of a SARS-CoV-2-infected individual reveals development of potent
303   neutralizing antibodies with limited somatic mutation. Immunity. 2020;53:98-105.
304   doi: 10.1101/2020.05.12.091298.

305   23.   Shi R, Shan C, Duan X, Chen Z, Liu P, Song J, et al. A human neutralizing
306   antibody targets the receptor binding site of SARS-CoV-2. Nature. 2020. Epub
307   2020/05/27. doi: 10.1038/s41586-020-2381-y. PubMed PMID: 32454512.

308   24.   Barnes CO, West AP, Huey-Tubman KE, Hoffmann MAG, Sharaf NG, Hoffman
309   PR, et al. Structures of human antibodies bound to SARS-CoV-2 spike reveal
310   common epitopes and recurrent features of antibodies. Cell. 2020. doi:
311   10.1016/j.cell.2020.06.025.

312   25.   Lv H, Wu NC, Tsang OT-Y, Yuan M, Perera RAPM, Leung WS, et al. Cross-
313   reactive antibody response between SARS-CoV-2 and SARS-CoV infections.
314   Cell Rep. 2020;31:107725. doi: (In Press).

315   26.   Zhou D, Duyvesteyn HME, Chen C-P, Huang C-G, Chen T-H, Shih S-R, et al.
316   Structural basis for the neutralization of SARS-CoV-2 by an antibody from a
317   convalescent patient. bioRxiv. 2020. doi: 10.1101/2020.06.12.148387.

318   27.   Wrapp D, Wang N, Corbett KS, Goldsmith JA, Hsieh CL, Abiona O, et al. Cryo-
319   EM structure of the 2019-nCoV spike in the prefusion conformation. Science.
320   2020;367:1260-3. Epub 2020/02/23. doi: 10.1126/science.abb2507. PubMed
321   PMID: 32075877.

322   28.   Ke Z, Oton J, Qu K, Cortese M, Zila V, McKeane L, et al. Structures,
323   conformations and distributions of SARS-CoV-2 spike protein trimers on intact
324   virions. bioRxiv. 2020. doi: 10.1101/2020.06.27.174979.

325   29.   Yao H, Song Y, Chen Y, Wu N, Xu J, Sun C, et al. Molecular architecture of the
326   SARS-CoV-2 virus. bioRxiv. 2020. doi: 10.1101/2020.07.08.192104.

327   30.   Klein JS, Bjorkman PJ. Few and far between: how HIV may be evading antibody
328   avidity. PLoS Pathog. 2010;6(5):e1000908. doi: 10.1371/journal.ppat.1000908.
329   PubMed PMID: 20523901; PubMed Central PMCID: PMCPMC2877745.

330   31.   Wrapp D, De Vlieger D, Corbett KS, Torres GM, Wang N, Van Breedam W, et al.
331   Structural basis for potent neutralization of betacoronaviruses by single-domain
332   camelid antibodies. Cell. 2020;181(5):1004-15 e15. Epub 2020/05/07. doi:
333   10.1016/j.cell.2020.04.031. PubMed PMID: 32375025; PubMed Central PMCID:
334   PMCPMC7199733.

335   32.   Ekiert DC, Kashyap AK, Steel J, Rubrum A, Bhabha G, Khayat R, et al. Cross-
336   neutralization of influenza A viruses mediated by a single antibody loop. Nature.

337   2012;489(7417):526-32. doi: 10.1038/nature11414. PubMed PMID: 22982990;
338   PubMed Central PMCID: PMCPMC3538848.

339 33. Lee PS, Yoshida R, Ekiert DC, Sakai N, Suzuki Y, Takada A, et al.
340   Heterosubtypic antibody recognition of the influenza virus hemagglutinin receptor
341   binding site enhanced by avidity. Proc Natl Acad Sci U S A. 2012;109(42):17040-
342   5. doi: 10.1073/pnas.1212371109. PubMed PMID: 23027945; PubMed Central
343   PMCID: PMCPMC3479480.

344 34. McLellan JS, Pancera M, Carrico C, Gorman J, Julien JP, Khayat R, et al.
345   Structure of HIV-1 gp120 V1/V2 domain with broadly neutralizing antibody PG9.
346   Nature. 2011;480(7377):336-43. Epub 2011/11/25. doi: 10.1038/nature10696.
347   PubMed PMID: 22113616; PubMed Central PMCID: PMCPMC3406929.

348 35. Pan J, Peng H, Chen B, Harrison SC. Cryo-EM structure of full-length HIV-1 Env
349   bound with the Fab of antibody PG16. J Mol Biol. 2020;432(4):1158-68. Epub
350   2020/01/14. doi: 10.1016/j.jmb.2019.11.028. PubMed PMID: 31931014; PubMed
351   Central PMCID: PMCPMC7058448.

352 36. Strauch EM, Bernard SM, La D, Bohn AJ, Lee PS, Anderson CE, et al.
353   Computational design of trimeric influenza-neutralizing proteins targeting the
354   hemagglutinin receptor binding site. Nat Biotechnol. 2017;35(7):667-71. doi:
355   10.1038/nbt.3907. PubMed PMID: 28604661; PubMed Central PMCID:
356   PMCPMC5512607.

357 37. Corti D, Voss J, Gamblin SJ, Codoni G, Macagno A, Jarrossay D, et al. A
358   neutralizing antibody selected from plasma cells that binds to group 1 and group
359   2 influenza A hemagglutinins. Science. 2011;333(6044):850-6. doi:
360   10.1126/science.1205669. PubMed PMID: 21798894.

361 38. Kadam RU, Juraszek J, Brandenburg B, Buyck C, Schepens WBG, Kesteleyn B,
362   et al. Potent peptidic fusion inhibitors of influenza virus. Science.
363   2017;358(6362):496-502. doi: 10.1126/science.aan0516. PubMed PMID:
364   28971971; PubMed Central PMCID: PMCPMC5659926.

365 39. Walls AC, Park YJ, Tortorici MA, Wall A, McGuire AT, Veesler D. Structure,
366   function, and antigenicity of the SARS-CoV-2 spike glycoprotein. Cell.
367   2020;181:281-92.e6. Epub 2020/03/11. doi: 10.1016/j.cell.2020.02.058. PubMed
368   PMID: 32155444.

369 40. Yuan M, Liu H, Wu NC, Lee C-CD, Zhu X, Zhao F, et al. Structural basis of a
370   shared antibody response to SARS-CoV-2. Science. 2020. doi:
371   10.1101/2020.06.08.141267. PubMed PMID: 32661058.

372 41. Bangaru S, Lang S, Schotsaert M, Vanderven HA, Zhu X, Kose N, et al. A site of
373   vulnerability on the influenza virus hemagglutinin head domain trimer interface.
374   Cell. 2019;177(5):1136-52.e18. Epub 2019/05/18. doi:
375   10.1016/j.cell.2019.04.011. PubMed PMID: 31100268.

376 42. Watanabe A, McCarthy KR, Kuraoka M, Schmidt AG, Adachi Y, Onodera T, et al.
377   Antibodies to a conserved influenza head interface epitope protect by an IgG

378   subtype-dependent mechanism. Cell. 2019;177(5):1124-35.e16. Epub
379   2019/05/18. doi: 10.1016/j.cell.2019.03.048. PubMed PMID: 31100267.

380   43.   Bajic G, Maron MJ, Adachi Y, Onodera T, McCarthy KR, McGee CE, et al.
381   Influenza antigen engineering focuses immune responses to a subdominant but
382   broadly protective viral epitope. Cell Host Microbe. 2019;25(6):827-35.e6. Epub
383   2019/05/21. doi: 10.1016/j.chom.2019.04.003. PubMed PMID: 31104946.

384   44.   Wu NC, Wilson IA. Structural insights into the design of novel anti-influenza
385   therapies. Nat Struct Mol Biol. 2018;25(2):115-21. doi: 10.1038/s41594-018-
386   0025-9. PubMed PMID: 29396418.

387   45.   Ward AB, Wilson IA. Innovations in structure-based antigen design and immune
388   monitoring for next generation vaccines. Curr Opin Immunol. 2020;65:50-6. Epub
389   2020/05/11. doi: 10.1016/j.coi.2020.03.013. PubMed PMID: 32387642; PubMed
390   Central PMCID: PMCPMC7174181.

391   46.   Menachery VD, Yount BL, Jr., Debbink K, Agnihothram S, Gralinski LE, Plante
392   JA, et al. A SARS-like cluster of circulating bat coronaviruses shows potential for
393   human emergence. Nat Med. 2015;21(12):1508-13. Epub 2015/11/10. doi:
394   10.1038/nm.3985. PubMed PMID: 26552008; PubMed Central PMCID:
395   PMCPMC4797993.

396   47.   Ekiert DC, Friesen RH, Bhabha G, Kwaks T, Jongeneelen M, Yu W, et al. A
397   highly conserved neutralizing epitope on group 2 influenza A viruses. Science.
398   2011;333(6044):843-50. doi: 10.1126/science.1204839. PubMed PMID:
399   21737702; PubMed Central PMCID: PMCPMC3210727.

400   48.   Otwinowski Z, Minor W. Processing of X-ray diffraction data collected in
401   oscillation mode. Methods Enzymol. 1997;276:307-26. Epub 1997/01/01.
402   PubMed PMID: 27754618.

403   49.   McCoy AJ, Grosse-Kunstleve RW, Adams PD, Winn MD, Storoni LC, Read RJ.
404   Phaser crystallographic software. J Appl Crystallogr. 2007;40(Pt 4):658-74. doi:
405   10.1107/S0021889807021206. PubMed PMID: 19461840; PubMed Central
406   PMCID: PMCPMC2483472.

407   50.   Fenn S, Schiller CB, Griese JJ, Duerr H, Imhof-Jung S, Gassner C, et al. Crystal
408   structure of an anti-Ang2 CrossFab demonstrates complete structural and
409   functional integrity of the variable domain. PLoS One. 2013;8(4):e61953. Epub
410   2013/04/25. doi: 10.1371/journal.pone.0061953. PubMed PMID: 23613981;
411   PubMed Central PMCID: PMCPMC3629102.

412   51.   Baden EM, Owen BA, Peterson FC, Volkman BF, Ramirez-Alvarado M,
413   Thompson JR. Altered dimer interface decreases stability in an amyloidogenic
414   protein. J Biol Chem. 2008;283(23):15853-60. Epub 2008/04/11. doi:
415   10.1074/jbc.M705347200. PubMed PMID: 18400753; PubMed Central PMCID:
416   PMCPMC2414275.

417   52.   Emsley P, Lohkamp B, Scott WG, Cowtan K. Features and development of Coot.
418   Acta Crystallogr D Biol Crystallogr. 2010;66(Pt 4):486-501. doi:

419   10.1107/S0907444910007493. PubMed PMID: 20383002; PubMed Central
420   PMCID: PMCPMC2852313.

421 53. Adams PD, Afonine PV, Bunkoczi G, Chen VB, Davis IW, Echols N, et al.
422   PHENIX: a comprehensive Python-based system for macromolecular structure
423   solution. Acta Crystallogr D Biol Crystallogr. 2010;66(Pt 2):213-21. Epub
424   2010/02/04. doi: 10.1107/S0907444909052925. PubMed PMID: 20124702;
425   PubMed Central PMCID: PMCPMC2815670.

426 54. Krissinel E, Henrick K. Inference of macromolecular assemblies from crystalline
427   state. J Mol Biol. 2007;372(3):774-97. Epub 2007/08/08. doi:
428   10.1016/j.jmb.2007.05.022. PubMed PMID: 17681537.

429 55. Suloway C, Pulokas J, Fellmann D, Cheng A, Guerra F, Quispe J, et al.
430   Automated molecular microscopy: the new Leginon system. J Struct Biol.
431   2005;151(1):41-60. Epub 2005/05/14. doi: 10.1016/j.jsb.2005.03.010. PubMed
432   PMID: 15890530.

433 56. Lander GC, Stagg SM, Voss NR, Cheng A, Fellmann D, Pulokas J, et al. Appion:
434   an integrated, database-driven pipeline to facilitate EM image processing. J
435   Struct Biol. 2009;166(1):95-102. PubMed PMID: 19263523; PubMed Central
436   PMCID: PMCPMC2775544.

437 57. Voss NR, Yoshioka CK, Radermacher M, Potter CS, Carragher B. DoG Picker
438   and TiltPicker: software tools to facilitate particle selection in single particle
439   electron microscopy. J Struct Biol. 2009;166(2):205-13. PubMed PMID:
440   19374019; PubMed Central PMCID: PMCPMC2768396.

441 58. Zivanov J, Nakane T, Forsberg BO, Kimanius D, Hagen WJ, Lindahl E, et al.
442   New tools for automated high-resolution cryo-EM structure determination in
443   RELION-3. eLife. 2018;7:e42166 Epub 2018/11/10. doi: 10.7554/eLife.42166.
444   PubMed PMID: 30412051; PubMed Central PMCID: PMCPMC6250425.

445 59. Schmidt F, Weisblum Y, Muecksch F, Hoffmann H-H, Michailidis E, Lorenzi JCC,
446   et al. Measuring SARS-CoV-2 neutralizing antibody activity using pseudotyped
447   and chimeric viruses. J Exp Med. 2020;217:e20201181. doi:
448   10.1101/2020.06.08.140871.

449 60. Edgar RC. MUSCLE: multiple sequence alignment with high accuracy and high
450   throughput. Nucleic Acids Res. 2004;32(5):1792-7. Epub 2004/03/23. doi:
451   10.1093/nar/gkh340. PubMed PMID: 15034147; PubMed Central PMCID:
452   PMCPMC390337.

453 61. Crooks GE, Hon G, Chandonia JM, Brenner SE. WebLogo: a sequence logo
454   generator. Genome Res. 2004;14(6):1188-90. doi: 10.1101/gr.849004. PubMed
455   PMID: 15173120; PubMed Central PMCID: PMCPMC419797.

456 62. Ashkenazy H, Abadi S, Martz E, Chay O, Mayrose I, Pupko T, et al. ConSurf
457   2016: an improved methodology to estimate and visualize evolutionary
458   conservation in macromolecules. Nucleic Acids Res. 2016;44(W1):W344-50.

459   Epub 2016/05/12. doi: 10.1093/nar/gkw408. PubMed PMID: 27166375; PubMed
460   Central PMCID: PMCPMC4987940.

461   63.   Wu NC, Yuan M, Liu H, Lee C-CD, Zhu X, Bangaru S, et al. An alternative
462   binding mode of IGHV3-53 antibodies to the SARS-CoV-2 receptor binding
463   domain. bioRxiv. 2020. doi: 10.1101/2020.07.26.222232.
464

465 **MATERIALS AND METHODS**

466 **Expression and purification of SARS-CoV-2 RBD**

467 The receptor-binding domain (RBD) (residues 319-541) of the SARS-CoV-2 spike (S)

468 protein (GenBank: QHD43416.1), and the RBD (residues 306-527) of the SARS-CoV S

469 protein (GenBank: ABF65836.1), were cloned into a customized pFastBac vector [47],

470 and fused with an N-terminal gp67 signal peptide and C-terminal His_6 tag [13]. For each

471 RBD, we further cloned a construct with an AviTag inserted in front of the His_6 tag. To

472 express the RBD, a recombinant bacmid DNA was generated using the Bac-to-Bac

473 system (Life Technologies). Baculovirus was generated by transfecting purified bacmid

474 DNA into Sf9 cells using FuGENE HD (Promega), and subsequently used to infect

475 suspension cultures of High Five cells (Life Technologies) at an MOI of 5 to 10. Infected

476 High Five cells were incubated at 28 °C with shaking at 110 r.p.m. for 72 h for protein

477 expression. The supernatant was then concentrated using a 10 kDa MW cutoff

478 Centramate cassette (Pall Corporation). The RBD protein was purified by Ni-NTA,

479 followed by size exclusion chromatography, and buffer exchanged into 20 mM Tris-HCl

480 pH 7.4 and 150 mM NaCl. For binding experiments, RBD with AviTag was biotinylated as

481 described previously [32] and purified by size exclusion chromatography on a Hiload 16/90

482 Superdex 200 column (GE Healthcare) in 20 mM Tris-HCl pH 7.4 and 150 mM NaCl.

483

484 **Expression and purification of Fabs**

485 Expression plasmids encoding the heavy and light chains of the COVA1-16 Fab were

486 transiently co-transfected into ExpiCHO cells at a ratio of 2:1 (HC:LC) using

487   ExpiFectamine™ CHO Reagent (Thermo Fisher Scientific) according to the

488   manufacturer's instructions. The supernatant was collected at 10 days post-transfection.

489   The Fabs were purified with a CaptureSelect™ CH1-XL Affinity Matrix (Thermo Fisher

490   Scientific) followed by size exclusion chromatography.

491

492   **Expression and purification of ACE2**

493   The N-terminal peptidase domain of human ACE2 (residues 19 to 615, GenBank:

494   BAB40370.1) was cloned into phCMV3 vector and fused with a C-terminal Fc tag. The

495   plasmids were transiently transfected into Expi293F cells using ExpiFectamine™ 293

496   Reagent (Thermo Fisher Scientific) according to the manufacturer's instructions. The

497   supernatant was collected at 7 days post-transfection. Fc-tagged ACE2 protein was then

498   purified with a Protein A column (GE Healthcare) followed by size exclusion

499   chromatography.

500

501   **Crystallization and x-ray structure determination**

502   The COVA1-16 Fab complex with RBD was formed by mixing each of the protein

503   components in an equimolar ratio and incubating overnight at 4°C. The COVA1-16

504   Fab/RBD complex and COVA1-16 Fab apo (unliganded) protein were adjusted to around

505   11 mg/mL and screened for crystallization using the 384 conditions of the JCSG Core

506   Suite (Qiagen) on our custom-designed robotic CrystalMation system (Rigaku) at Scripps

507   Research. Crystallization trials were set-up by the vapor diffusion method in sitting drops

508   containing 0.1 µl of protein and 0.1 µl of reservoir solution. Crystals used for x-ray data

509   collection were harvested from drops containing 0.2 M sodium iodide and 20% (w/v)

510   polyethylene glycol 3350 for the COVA1-16 Fab/RBD complex and from drops containing

511   0.08 M acetate pH 4.6, 20% (w/v) polyethylene glycol 4000, 0.16 M ammonium sulfate

512   and 20% (v/v) glycerol for the COVA1-16 Fab. Crystals appeared on day 3, were

17

513   harvested on day 7, pre-equilibrated in cryoprotectant containing 20% glycerol, and then

514   flash cooled and stored in liquid nitrogen until data collection. Diffraction data were

515   collected at cryogenic temperature (100 K) at Stanford Synchrotron Radiation Lightsource

516   (SSRL) on the new Scripps/Stanford beamline 12-1 with a beam wavelength of 0.97946

517   Å, and processed with HKL2000 [48]. Structures were solved by molecular replacement

518   using PHASER [49]. The models for molecular replacement of RBD and COVA1-16 were

519   from PDB 6XC4 [40], 4IMK [50] and 2Q20 [51]. Iterative model building and refinement

520   were carried out in COOT [52] and PHENIX [53], respectively. Epitope and paratope

521   residues, as well as their interactions, were identified by accessing PISA at the European

522   Bioinformatics Institute (http://www.ebi.ac.uk/pdbe/prot_int/pistart.html) [54].

523

524   **Expression and purification of recombinant S proteins**

525   The SARS-CoV-2 S construct used for negative stain EM contains the mammalian-codon-

526   optimized gene encoding residues 1-1208 of the S protein (GenBank: QHD43416.1),

527   followed by a C-terminal T4 fibritin trimerization domain, an HRV3C cleavage site, 8x-His

528   tag and a Twin-strep tags subcloned into the eukaryotic-expression vector pcDNA3.4.

529   Three amino-acid mutations were introduced into the S1/S2 cleavage site (RRAR to

530   GSAS) to prevent cleavage and two stabilizing proline mutations (K986P and V987P) to

531   the HR1 domain. For additional S stabilization, residues T883 and V705 were mutated to

532   cysteines to introduce a disulphide bond. The S plasmid was transfected into 293F cells

533   and supernatant was harvested at 6 days post transfection. S protein was purified by

534   running the supernatant through a streptactin column and then by size exclusion

535   chromatography using a Superose 6 increase 10/300 column (GE Healthcare

536   Biosciences). Protein fractions corresponding to the trimeric S protein were collected and

537   concentrated.

538

539 **ns-EM sample preparation and data collection**

540 SARS-COV-2 S protein was complexed with 3x molar excess of Fab at 30 minutes prior

541 to direct deposition onto carbon-coated 400-mesh copper grids. The grids were stained

542 with 2 % (w/v) uranyl-formate for 90 seconds immediately following sample application.

543 Grids were either imaged at 200 KeV or at 120 KeV on a Tecnai T12 Spirit using a 4kx4k

544 Eagle CCD. Micrographs were collected using Leginon [55] and the images were

545 transferred to Appion for processing. Particle stacks were generated in Appion [56] with

546 particles picked using a difference-of-Gaussians picker (DoG-picker) [57]. Particle stacks

547 were then transferred to Relion [58] for 2D classification followed by 3D classification to

548 sort well-behaved classes. Selected 3D classes were auto-refined on Relion and used to

549 make figures with UCSF Chimera.

550

551 **Protein expression and purification for antibody binding studies**

552 All constructs were expressed transiently in HEK293F (Invitrogen, cat no. R79009) cells

553 maintained in Freestyle medium (Life Technologies). For soluble RBD proteins, cells were

554 transfected at a density of 0.8-1.2 million cells/mL by addition of a mix of PEImax (1 µg/µL)

555 with expression plasmids (312.5 µg/L) in a 3:1 ratio in OptiMEM. Supernatants of the

556 soluble RBD proteins were harvested six days post transfection, centrifuged for 30 min at

557 4000 rpm and filtered using 0.22 µm Steritop filters (Merck Millipore). Constructs with a

558 His$_6$-tag were purified by affinity purification using Ni-NTA agarose beads. Protein eluates

559 were concentrated, and buffer exchanged to PBS using Vivaspin filters with a 10 kDa

560 molecular weight cutoff (GE Healthcare). Protein concentrations were determined by

561 Nanodrop using the proteins peptidic molecular weight and extinction coefficient as

562 determined by the online ExPASy software (ProtParam). For the COVA1-16 IgG1

563 antibody, suspension HEK293F cells (Invitrogen, cat no. R79007) were cultured in

564 FreeStyle medium (Gibco) and co-transfected with the two IgG plasmids expressing the

19

565   corresponding HC and LC in a 1:1 ratio at a density of 0.8-1.2 million cells/mL in a 1:3

566   ratio with 1 mg/L PEImax (Polysciences). The recombinant IgG antibodies were isolated

567   from the cell supernatant after five days as described previously (20, 48). In short, the cell

568   suspension was centrifuged 25 min at 4000 rpm, and the supernatant was filtered using

569   0.22 µm pore size SteriTop filters (Millipore). The filtered supernatant was run over a 10

570   mL protein A/G column (Pierce) followed by two column volumes of PBS wash. The

571   antibodies were eluted with 0.1 M glycine pH 2.5, into the neutralization buffer of 1 M TRIS

572   pH 8.7 in a 1:9 ratio. The purified antibodies were buffer exchanged to PBS using 100 kDa

573   VivaSpin20 columns (Sartorius). The IgG concentration was determined on the NanoDrop

574   2000 and the antibodies were stored at 4°C until further analyses.

575

576   **Measurement of binding affinities using biolayer interferometry**

577   To determine the binding affinity of COVA1-16 IgG and His-tagged Fabs, 20 µg/mL of His-

578   tagged SARS-CoV or SARS-CoV-2 RBD protein in running buffer (PBS, 0.02% Tween-

579   20, 0.1% BSA) was loaded on Ni-NTA biosensors (ForteBio) for 300 s. Streptavidin

580   biosensors (ForteBio) were used if the RBD was biotinylated. Next, the biosensors were

581   transferred to running buffer containing IgG or Fab to determine the association rate, after

582   which the sensor was transferred to a well containing running buffer to allow dissociation.

583   As negative control, an anti-HIV-1 His-tagged Fab was tested at the highest concentration

584   used for COVA1-16 Fab (400 nM). After each cycle, the sensors were regenerated by

585   alternating 20 mM glycine in PBS and running buffer three times, followed by reactivation

586   in 20 mM NiCl$_2$ for 120 s. All steps were performed at 1000 rpm shaking speed. K$_{DS}$ were

587   determined using ForteBio Octet CFR software. The avidity effects of IgG were

588   investigated by titrating the SARS-CoV-2 RBD concentration (5, 1, 0.2 and 0.04 µg/mL)

589   followed by loading on Ni-NTA biosensors for 480 s with an additional loading step with

590 His-tagged HIV-1 gp41 for 480 s to minimize background binding of His-tagged Fabs to

591 the biosensor. All other steps were performed as described above.

592

593 **Competition studies of antibodies with ACE-2 receptor**

594 For competition assays, COVA1-16 IgG, CR3022 IgG, and human ACE2-Fc were all

595 diluted to 250 nM. Ni-NTA biosensors were used. In brief, the assay has five steps: 1)

596 baseline: 60 s with 1x kinetics buffer; 2) loading: 180 s with 20 µg/mL, His_6-tagged SARS-

597 CoV-2 RBD proteins; 3) baseline: 150 s with 1x kinetics buffer; 4) first association: 300 s

598 with CR3022 IgG or human ACE2-Fc; and 5) second association: 300 s with human ACE2-

599 Fc, CR3022 IgG, or COVA1-16 IgG.

600

601 **Pseudovirus neutralization assay**

602 Neutralization assays were performed using SARS-CoV and SARS-CoV-2 S-

603 pseudotyped HIV-1 virus and HEK-293T/ACE2 cells as described previously [59]. In brief,

604 pseudotyped virus was produced by co-transfecting expression plasmids of SARS-CoV S

605 and SARS-CoV-2$_{\Delta19}$ S proteins (GenBank; AAP33697.1 and MT449663.1, respectively)

606 with an HIV backbone expressing NanoLuc luciferase (pHIV-1$_{NL4-3}$ ΔEnv-NanoLuc) in

607 HEK293T cells (ATCC, CRL-11268). After 3 days, the cell culture supernatants containing

608 SARS-CoV and SARS-CoV-2 S-pseudotyped HIV-1 viruses were stored at -80℃. HEK-

609 293T/ACE2 cells were seeded 10,000 cells/well in a 96-well plate one day prior to the start

610 of the neutralization assay. To determine the neutralizing capacity of COVA1-16 IgG and

611 His_6-tagged Fab, 20 or 100 µg/mL COVA1-16 IgG and equal molar of COVA1-16 Fab

612 were serially diluted in 3-fold steps and mixed with SARS-CoV or SARS-CoV-2

613 pseudotyped virus and incubated for 1 h at 37°C. The pseudotyped virus and COVA1-16

614 IgG/Fab mix were then added to the HEK-293T/ACE2 cells and incubated at 37°C. After

615 48 h, cells were washed twice with PBS (Dulbecco's Phosphate-Buffered Saline,

21

616   eBiosciences) and lysis buffer was added. Luciferase activity of cell lysate was measured

617   using the Nano-Glo Luciferase Assay System (Promega) and GloMax Discover System.

618   The inhibitory concentration (IC$_{50}$) was determined as the concentration of IgG or Fab that

619   neutralized 50% of the pseudotyped virus using GraphPad Prism software (version 8.3.0).

620

621   **Sequence conservation analysis**

622   RBD protein sequences from SARS-CoV and SARS-related coronavirus (SARSr-CoV)

623   strains were retrieved from the following accession codes:

624   • GenBank ABF65836.1 (SARS-CoV)

625   • GenBank ALK02457.1 (Bat SARSr-CoV WIV16)

626   • GenBank AGZ48828.1 (Bat SARSr-CoV WIV1)

627   • GenBank ACU31032.1 (Bat SARSr-CoV Rs672)

628   • GenBank AIA62320.1 (Bat SARSr-CoV GX2013)

629   • GenBank AAZ67052.1 (Bat SARSr-CoV Rp3)

630   • GenBank AIA62300.1 (Bat SARSr-CoV SX2013)

631   • GenBank ABD75323.1 (Bat SARSr-CoV Rf1)

632   • GenBank AIA62310.1 (Bat SARSr-CoV HuB2013)

633   • GenBank AAY88866.1 (Bat SARSr-CoV HKU3-1)

634   • GenBank AID16716.1 (Bat SARSr-CoV Longquan-140)

635   • GenBank AVP78031.1 (Bat SARSr-CoV ZC45)

636   • GenBank AVP78042.1 (Bat SARSr-CoV ZXC21)

637   • GenBank QHR63300.2 (Bat CoV RaTG13)

638   • NCBI Reference Sequence YP_003858584.1 (Bat SARSr-CoV BM48-31)

639   • GISAID EPI_ISL_410721 (Pangolin BetaCoV Guandong2019)

640   Multiple sequence alignment of the RBD sequences was performed by MUSCLE version

641   3.8.31 [60]. Sequence logos were generated by WebLogo [61]. The conservation score

642   of each RBD residue was calculated and mapped onto the SARS-CoV-2 RBD x-ray

643   structure with ConSurf [62].

644   **ACKNOWLEDGEMENTS**

663

664 **AUTHOR CONTRIBUTIONS**

665 H.L., N.C.W., M.Y. and I.A.W. conceived and designed the study. H.L., N.C.W., M.Y., and

666 C.C.D.L. expressed and purified the proteins for crystallization. T.G.C., P.J.M.B., M.J.v.G.

667 and R.W.S. provided antibody clones and sequences. T.G.C. performed binding analyses

668 and J.v.S. provided neutralization data. H.L., N.C.W., M.Y. and X.Z. crystallized and

669 determined the X-ray structures. S.B., J.L.T., and A.B.W. provided nsEM data and

670 reconstructions. H.L., N.C.W., M.Y., and I.A.W. wrote the paper and all authors reviewed

671 and/or edited the paper.

672

673 **COMPETING INTERESTS**

674 Amsterdam UMC previously filed a patent application on the SARS-CoV-2 antibody

675 COVA1-16 described here [6].

676

677 **DATA AVAILABILITY**

678 X-ray coordinates and structure factors are being deposited to the RCSB Protein Data

679 Bank. The COVA1-16 IGVH and IGVK sequences are available in GenBank: MT599919

680 and MT599835. The plasmids encoding the COVA1-16 IgG and Fab will be available from

681 M.J.v.G. and R.W.S. under an MTA with the Amsterdam UMC. Other materials related to

682 this paper will be available on request from the corresponding author.

683
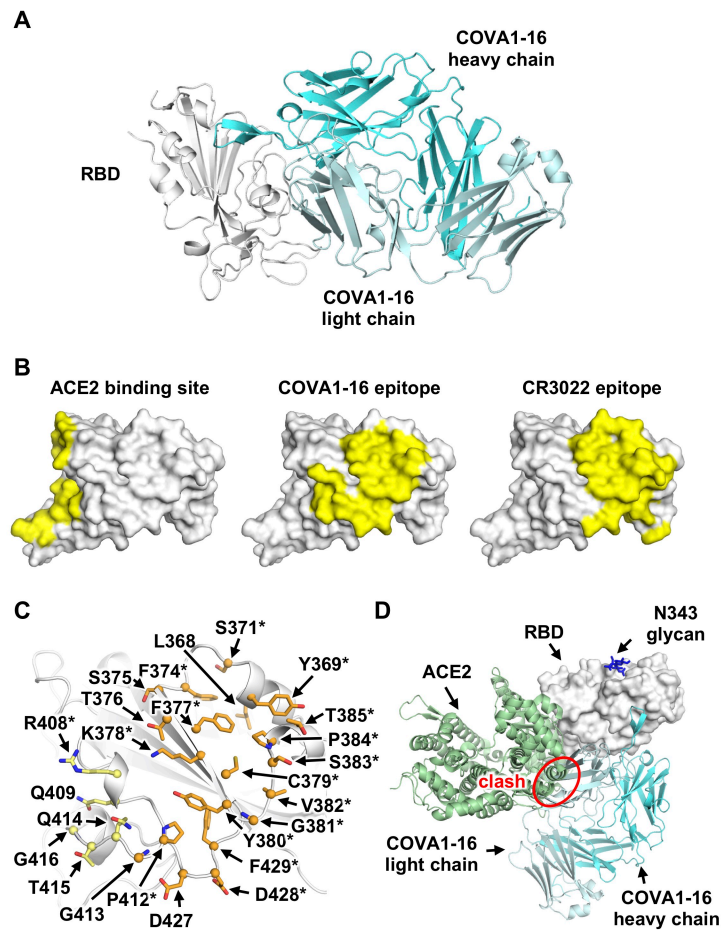
Figure 1. Comparison of COVA1-16 binding mode with CR3022 and ACE2. (A) Crystal structure of COVA1-16/RBD complex with RBD in grey and COVA1-16 Fab in cyan (heavy chain) and greyish blue (light chain). **(B)** ACE2-binding site (PDB 6M0J, left) [10], COVA1-16 epitope (this study, middle), and CR3022 epitope (PDB 6W41, right) [13] are highlighted in yellow. **(C)** RBD residues in the COVA1-16 epitope are shown. Epitope residues contacting the heavy chain are in orange and light chain in yellow. Representative epitope residues are labeled. Residues that are also part of CR3022 epitope are indicated with asterisks. **(D)** The ACE2/RBD complex structure is aligned in the same orientation as the COVA1-16/RBD complex. COVA1-16 (cyan) would clash with ACE2 (green) if they were to approach their respective RBD binding sites at the same time (indicated by red circle).
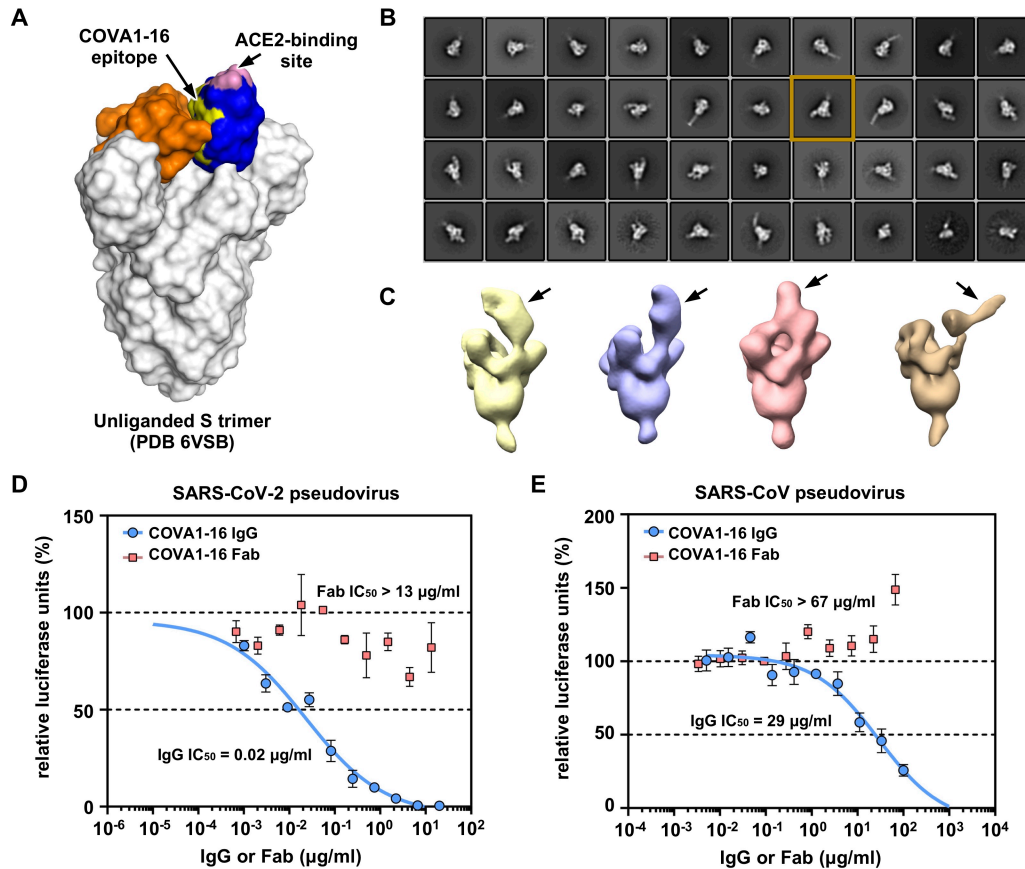
Figure 2. Negative-stain electron microscopy analysis and IgG avidity effect of COVA1-16. (A) The COVA1-16 epitope on the unliganded SARS-CoV-2 S trimer with one RBD in the "up" conformation (blue) and two in the "down" conformation (orange) (PDB 6VSB) [27]. COVA1-16 epitope is in yellow and ACE2-binding site in pink. **(B)** Representative 2D class averages from negative-stain EM analysis of SARS-CoV-2 S trimer complexed with COVA1-16 Fab. The 2D class corresponding to the most outward conformation of COVA-16 Fab in complex with S trimer is highlighted in a mustard box. **(C)** Various conformations of COVA1-16 Fab in complex with the S trimer is revealed by 3D reconstructions. The location of COVA1-16 Fab is indicated by an arrow. **(D-E)** Neutralization activities of COVA1-16 IgG (blue) and Fab (red) against **(D)** SARS-CoV-2 and **(E)** SARS-CoV ar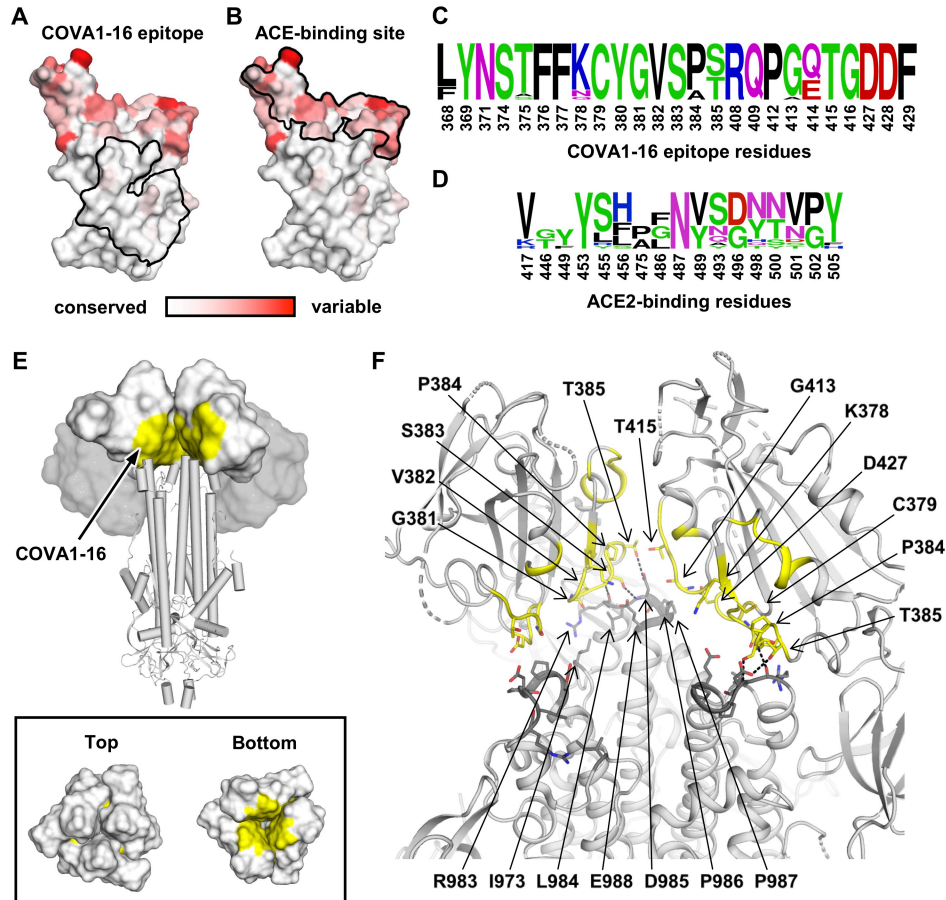e measured in a luciferase-based pseudovirus assay. The half maximal inhibitory concentrations (IC_{50}s) for IgG and Fab are indicated in parenthesis. Of

26

708   note, neutralization for the IgG (IC_{50} = 0.08 µg/mL) against SARS-CoV-2 pseudovirus

709   infecting 293T/ACE2 cells is comparable to that measured in Huh7 cells (IC_{50} = 0.13

710   µg/mL) as reported previously [6].

27
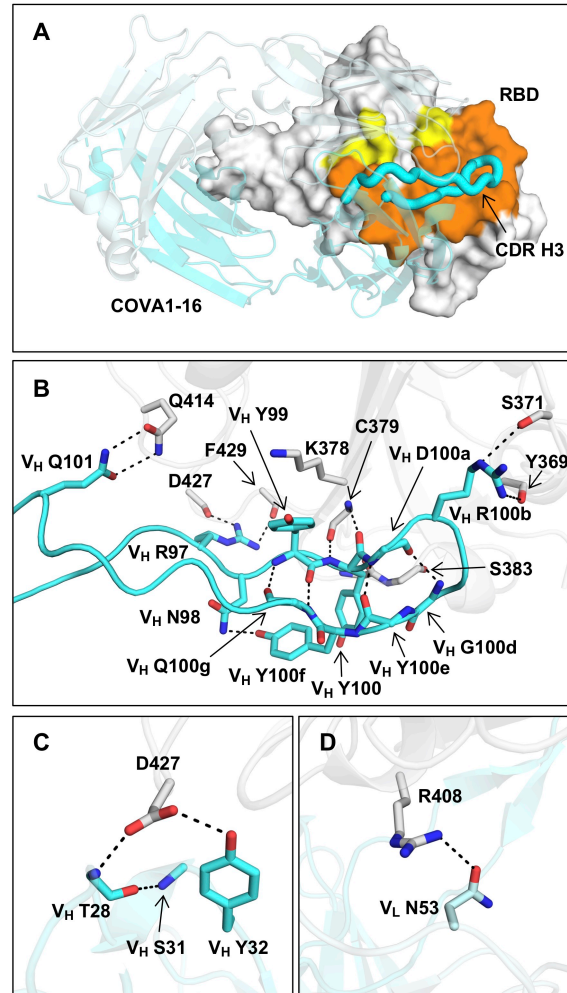
Figure 3. Interaction between SARS-CoV-2 RBD and COVA1-16. (A) The epitope of COVA1-16 is highlighted in yellow and orange. Epitope residues that are in contact with CDR H3 are in orange, and yellow otherwise. COVA1-16 (cyan) is in cartoon representation with CDR H3 depicted in a thick tube. The RBD (white) is in a surface representation. The BSA on COVA1-16 and RBD are 844 Å^2 and 779 Å^2, respectively. **(B)** Interactions of SARS-CoV-2 RBD (white) with **(B)** CDR H3, **(C)** CDR H1, and **(D)** CDR L2 of COVA1-16 (cyan) are shown. Hydrogen bonds are represented by dashed lines. In **(C)**, a 3_{10} turn is observed in CDR H1 for residues V_H T28 to V_H S31.
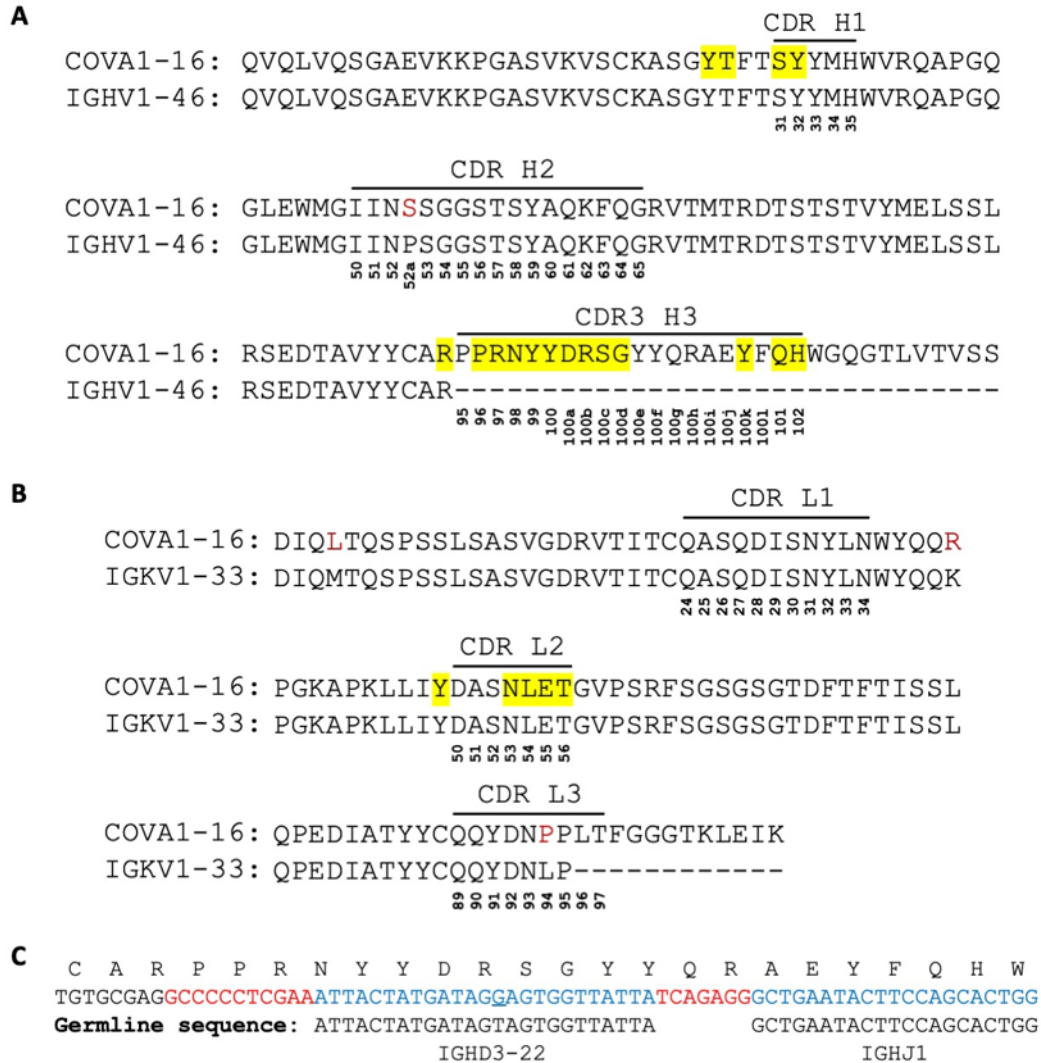
Figure 4. Sequence conservation of COVA1-16 epitope and ACE2-binding site. (A-B) Sequence conservation of the RBD among 17 SARS-like CoVs (Figure S7) is highlighted on the RBD structure with the **(A)** COVA1-16 epitope and **(B)** ACE2-binding site indicated by the black outline. The backside of this view is shown in Figure S8. **(C-D)** Sequence conservation of **(C)** COVA1-16 epitope and **(D)** ACE2-binding site is shown as a sequence logo. **(E)** Location of COVA1-16 epitope (yellow) on the SARS-CoV-2 S trimer when all three RBDs are in the down conformation (PDB 6VXX) [39]. RBDs are represented as a white surface, N-terminal domains (NTDs) as a grey surface, and the S2 domain in a cartoon representation. Top panel: for visualization of the COVA1-16 epitope, the RBD and NTD from one of the three protomers was removed. Bottom panel: top and bottom views of the COVA1-16 epitopes on the three RBDs in the "down" conformation. **(F)** COVA1-16 epitope is shown in yellow on a ribbon representation of a SARS-CoV-2 S

29

733   trimer (PDB 6VXX) [39]. Epitope residues in the RBD involved in interaction with the S2

734   domain are shown in yellow sticks, and S2 domain interacting residues in dark grey sticks.

735   Dashed lines indicate hydrogen bonds. Interface residues are calculated using PISA [54].

736   The S1 segment from the third protomer is omitted to clarify the view of the interfaces that

737   the COVA1-16 epitope makes with the S2 domain.

738
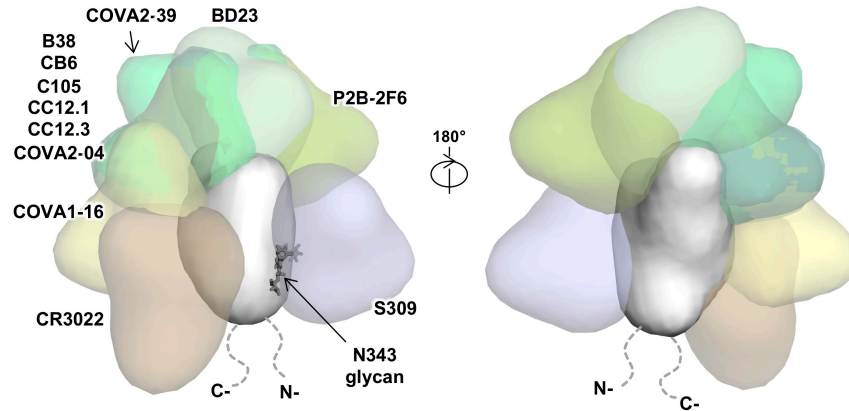
Figure 5. Interaction between SARS-CoV-2 RBD and structurally characterized antibodies. The binding of known SARS-CoV-2 RBD-targeting antibodies to the RBD is compared. The ACE2-binding site overlaps with epitopes of B38 (PDB 7BZ5) [20], C105 (6XCM) [24], CB6 (7C01) [23], CC12.1 (6XC3) [40], CC12.3 (6XC4) [40], BD23 (7BYR) [7], and P2B-2F6 (7BWJ) [19], but not the epitopes of COVA1-16 (this study), CR3022 (PDB 6W41) [13], COVA2-04 [63], COVA2-39 [63], and S309 (PDB 6WPS) [18]. Of note, while CR3022 only neutralizes SARS-CoV but not SARS-CoV-2 in *in vitro* assays [13], a recent study isolated an antibody (EY6A) that binds to a similar epitope as CR3022 and cross-neutralizes SARS-CoV-2 and SARS-CoV [26].

A

CDR H1

COVA1-16: QVQLVQSGAEVKKPGASVKVSCKASGYTFTSYYMHWVRQAPGQ
IGHV1-46: QVQLVQSGAEVKKPGASVKVSCKASGYTFTSYYMHWVRQAPGQ
31 32 33 34 35

CDR H2

COVA1-16: GLEWMGIINSSGGSTSYAQKFQGRVTMTRDTSTSTVYMELSSL
IGHV1-46: GLEWMGIINPSGGSTSYAQKFQGRVTMTRDTSTSTVYMELSSL
50 51 52 52a 53 54 55 56 57 58 59 60 61 62 63 64 65

CDR3 H3

COVA1-16: RSEDTAVYYCARPPRNYYDRSGYYQRAEYFQHWGQGTLVTVSS
IGHV1-46: RSEDTAVYYCAR-------------------------------
95 96 97 98 99 100 100a 100b 100c 100d 100e 100f 100g 100h 100i 100j 100k 100l 101 102

B

CDR L1

COVA1-16: DIQLTQSPSSLSASVGDRVTITCQASQDISNYLNWYQQR
IGKV1-33: DIQMTQSPSSLSASVGDRVTITCQASQDISNYLNWYQQK
24 25 26 27 28 29 30 31 32 33 34

CDR L2

COVA1-16: PGKAPKLLIYDASNLETGVPSRFSGSGSGTDFTFTISSL
IGKV1-33: PGKAPKLLIYDASNLETGVPSRFSGSGSGTDFTFTISSL
50 51 52 53 54 55 56

CDR L3

COVA1-16: QPEDIATYYCQQYDNPPLTFGGGTKLEIK
IGKV1-33: QPEDIATYYCQQYDNLP------------
89 90 91 92 93 94 95 96 97

C

```
     C   A   R   P   P   R   N   Y   Y   D   R   S   G   Y   Y   Q   R   A   E   Y   F   Q   H   W
     TGTGCGAGGCCCCCTCGAAATTACTATGATAGGAGTGGTTATTATCAGAGGGCTGAATACTTCCAGCACTGG
     Germline sequence: ATTACTATGATAGTAGTGGTTATTA        GCTGAATACTTCCAGCACTGG
                     IGHD3-22                              IGHJ1
```

Total gene-derived nucleotides: 46
Total non-gene-derived nucleotides: 18

1

2 **Supplementary Figure 1. Comparison of COVA1-16 and putative germline**

3 **sequences.** Alignment of COVA1-16 Fab amino-acid sequence with **(A)** germline IGHV1-

4 46 sequence, and **(B)** germline IGKV1-33 sequence. The regions that correspond to CDR

5 H1, H2, H3, L1, L2, and L3 are indicated. Residues that differ from germline are highlighted

6 in red. COVA1-16 Fab residues that interact with the RBD are highlighted in yellow.

7 Residue positions in the CDRs are labeled according to the Kabat numbering scheme. **(C)**

8 Amino acid and nucleotide sequences of the V-D-J junction of COVA1-16, with putative

9   gene segments (blue) and N-regions (red), are indicate. The germline sequences of

10   IGHD3-22 and IGHJ1 are also shown. The only somatically mutated nucleotide in the D

11   region is underlined.

12
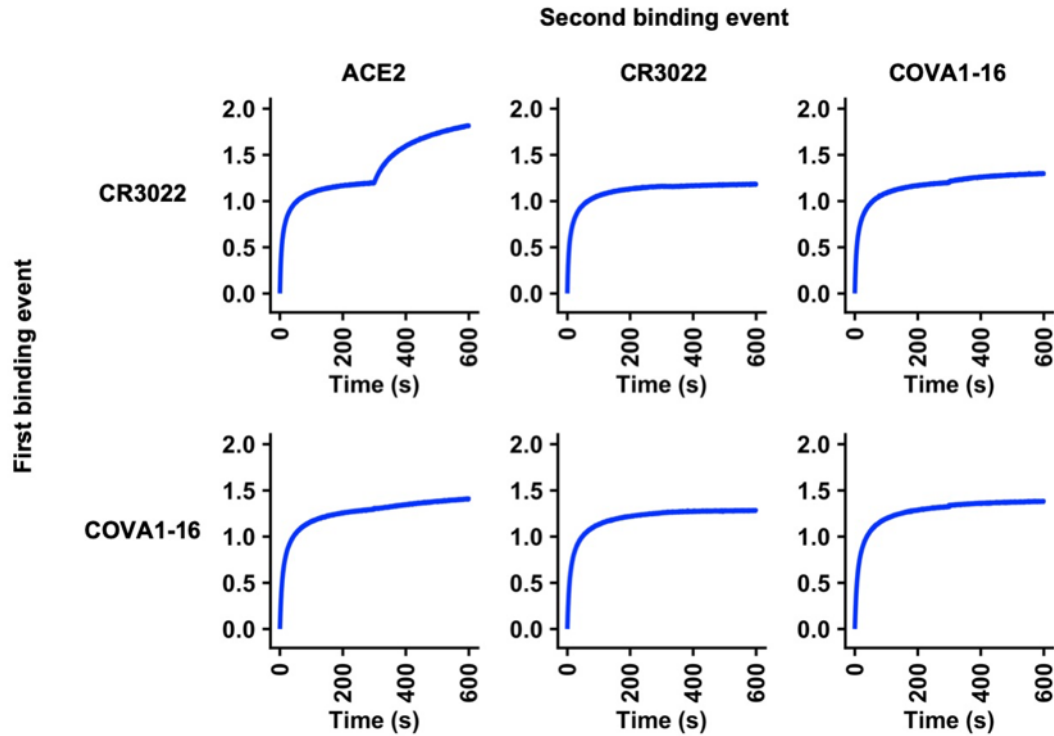
Supplementary Figure 2. Competition assay between different IgGs and ACE2.

Competition between COVA1-16 IgG, CR3022 IgG, and Fc-tagged ACE2 was measured

by biolayer interferometry (BLI). Y-axis represents the response. The biosensor was first

loaded with SARS-CoV-2 RBD, followed by two binding events: 1) CR3022 IgG or

COVA1-16 IgG, and 2) ACE2, CR3022 IgG, or COVA1-16 IgG. A period of 300 s was

used for each binding event. A further increase in signal during the second binding event

(starting at 300 s time point) indicates lack of competition with the first ligand.

20

21

22
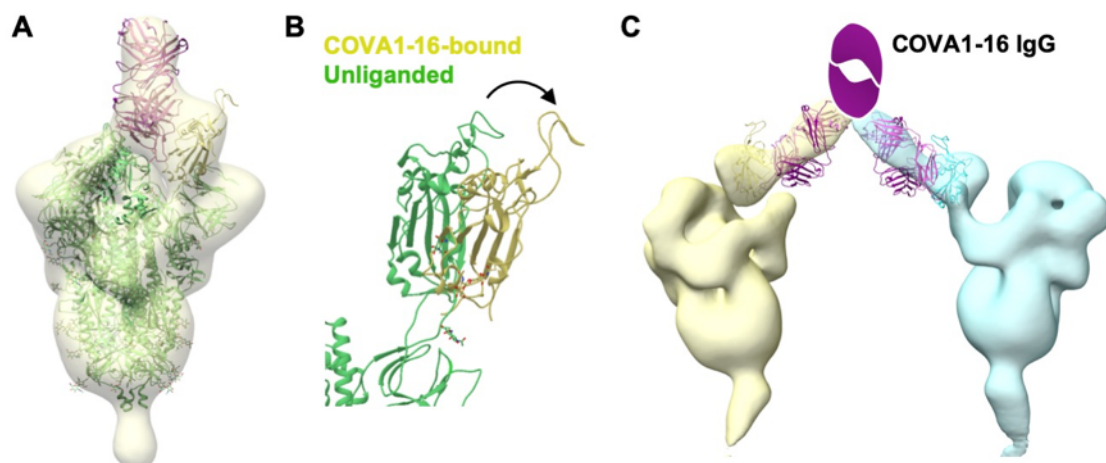
Supplementary Figure 3. Negative-stain EM analysis of COVA1-16 binding to SARS-CoV-2 S trimer. (A) An atomic model from the crystal structure of SARS-CoV-2 RBD bound to COVA1-16 Fab was fit into the negative-stain EM reconstruction of the SARS-CoV-2 spike bound to COVA1-16 Fab. The COVA1-16 Fab approaches the apex of the S trimer in a perpendicular orientation. A secondary structure backbone representation of the prefusion spike model (PDB: 6Z97, green) [1] was also fit into the EM density with RBD residues (334-528) removed from one of the protomers here for clarity. The COVA1-16 heavy and light chains are in magenta and pink, respectively, and COVA1-16-bound RBD in yellow. **(B)** Conformation of RBD in an up conformation from an unliganded SARS-CoV-2 S trimer (PDB: 6Z97, green) [1] is compared to that of the RBD (yellow) bound by COVA1-16 Fab. The arrow indicates that the RBD further rotates and opens up when bound to COVA1-16, thereby moving further away from the trimer threefold axis. **(C)** An atomic model of the spike RBD bound to COVA1-16 Fab is fit into a negative-stain EM reconstruction, where COVA1-16 Fab approaches the SARS-CoV-2 S trimer from the side. COVA1-16 is modelled as an IgG to illustrate the feasibility of bivalent binding to adjacent spike proteins on the virus surface. The Fab heavy and light chains are shown in magenta and pink. A schematic representation of the Fc domain of the IgG is shown in

4

5

40   magenta. The RBD model and spike density for each trimer is shown in yellow and cyan.

41
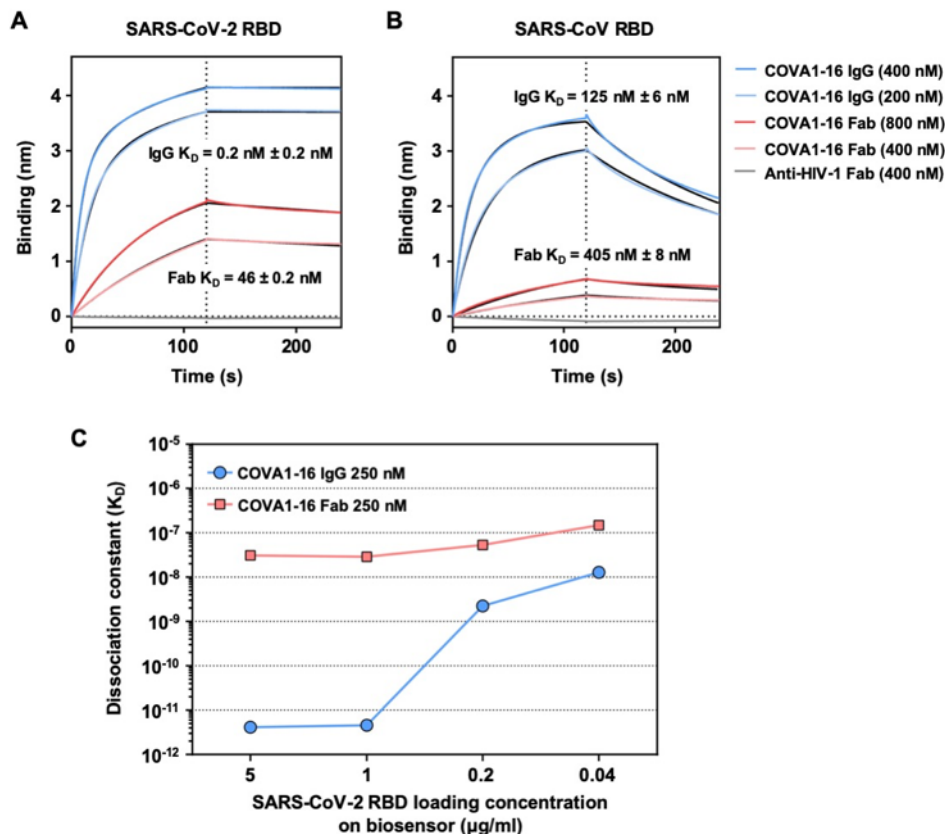
Supplementary Figure 4. Sensorgrams for binding of COVA1-16 to SARS-CoV-2

RBD and SARS-CoV RBD. (A-B) Binding kinetics of COVA1-16 Fab and IgG to **(A)**

SARS-CoV-2 RBD and **(B)** SARS-CoV RBD were measured by biolayer interferometry

(BLI) with RBD on the biosensor and antibody in solution. Y-axis represents the response.

An anti-HIV His-tagged Fab (4E1) was used as a negative control. Dissociation constants

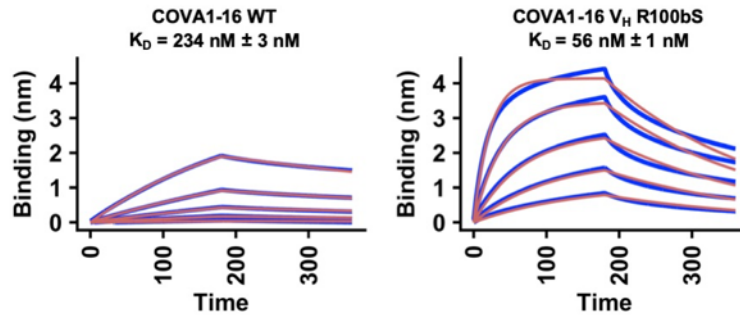(K_D) for IgG and Fab were obtained using a 1:2 bivalent model and 1:1 binding model,

respectively, which are represented by the black lines. Representative results of two

replicates for each experiment are shown. **(C)** The relationship between SARS-CoV-2

RBD loading concentration on the biosensor and the dissociation constant of COVA1-16

IgG is shown.

52

6

53

Supplementary Figure 5. Sensorgrams for binding of COVA1-16 wild-type and V_H R100bS mutant Fabs to SARS-CoV-2 RBD. Binding kinetics of COVA1-16 wild-type and V_H R100bS mutant Fab to SARS-CoV-2 RBD were measured by biolayer interferometry (BLI) with RBD on the biosensor and antibody in solution. Y-axis represents the response. Dissociation constants (K_D) for Fabs were obtained using a 1:1 binding model, which are represented by the red lines. Representative results of two replicates for each experiment are shown. Unlike Figure S4, which used HEK293F-expressed SARS-CoV-2, the experiment here used insect cell-expressed SARS-CoV-2.

7
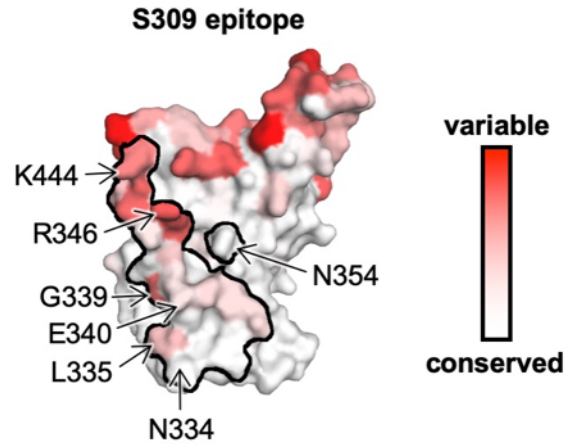
62
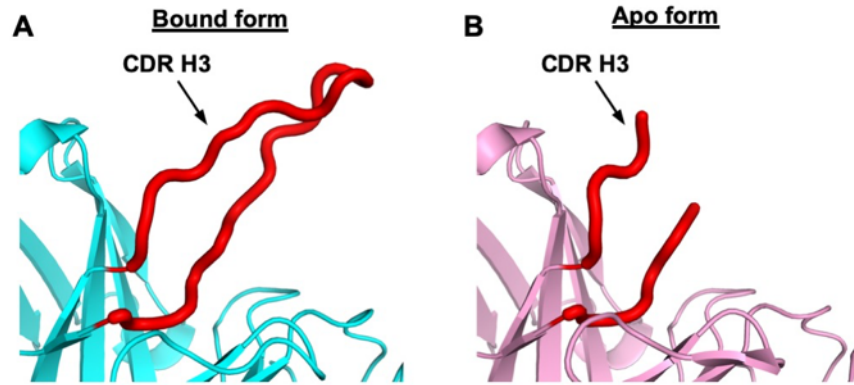
Supplementary Figure 6. CDR H3 of COVA1-16 Fab is disordered in its unliganded

apo form. (A) In the crystal structure of the RBD-bound form of COVA1-16 Fab, the

CDR H3 loop is completely ordered (red). **(B)** In the crystal structure of the apo form of

COVA1-16, the distal end of the CDR H3 loop is intrinsically disordered or flexible (red).

8

67

Supplementary Figure 7. Sequence alignment of the RBD from SARS-related coronaviruses. Amino-acid sequences of RBDs from SARS-CoV-2, SARS-CoV, and other SARS-related coronavirus (SARSr-CoV) strains are aligned. COVA1-16 epitope residues are highlighted in cyan. ACE2-binding residues are highlighted in purple. Conserved residues are indicated by small black dots on the top of the alignment.

68
69
70
71
72

S309 epitope

73

74   **Supplementary Figure 8. Sequence conservation of S309 epitope.** Sequence

75   conservation of the RBD is highlighted on the structure for S309 epitope [2]. This view

76   corresponds to the opposite side (rotated 180 degrees along the vertical axis) from that
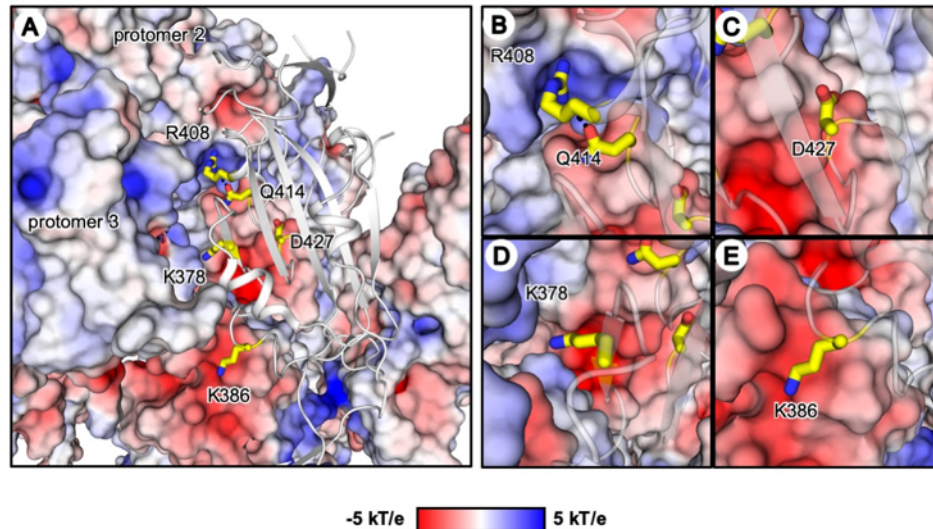
77   shown in Figure 4A-B.

78

COVA1-16 epitope

-5 kT/e ▭ 5 kT/e
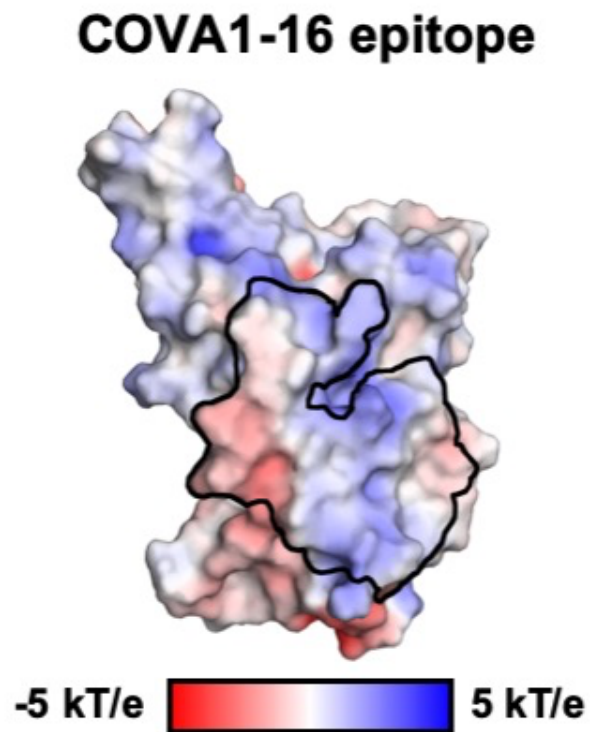
79

80   **Supplementary Figure 9. COVA1-16 epitope in electrostatic surface representation.**

81   The epitope of COVA1-16 is outlined and shows its largely polar nature.

-5 kT/e ▭ 5 kT/e

82

Supplementary Figure 10. Location of residues of interest in the COVA1-16 epitope when all three RBDs are in the "down" conformation. (A) The RBD of one of the three protomers is shown as a gray cartoon with the side chains of five residues of interest shown in yellow stick representation. RBD residues K378, R408, Q414, and D427 are within the COVA1-16 epitope, whereas K386 is not a COVA1-16 epitope residue. The other two protomers (protomers 2 and 3) are shown in a surface electrostatic representation. **(B-E)** Zoomed-in views for the regions surrounding residues **(B)** R408 and Q414, **(C)** D427, **(D)** K378, and **(E)** K386**.** A hydrogen bond in **(B)** is represented by a dashed line. Due to charge difference or similarity between the side chain and the proximal region of the neighboring protomer, either repulsive (same charge) or attractive (opposite charge) environments are found and visualized here. PDB 6VXX is used to represent the spike protein [3]. Of note, the shape complementarity values (Sc) [4] of the COVA1-16 epitope/RBD interface, COVA1-16 epitope/S2 interface, and COVA1-16 epitope/COVA1-16 interface are 0.53, 0.75, and 0.74, respectively, indicating good complementary and tight fit of the COVA1-16 epitope surface with the rest of the trimer in the RBD down

98   conformation. Sc values can range from 0 to 1, with a larger Sc value represents higher

99   shape complementarity.

100

101
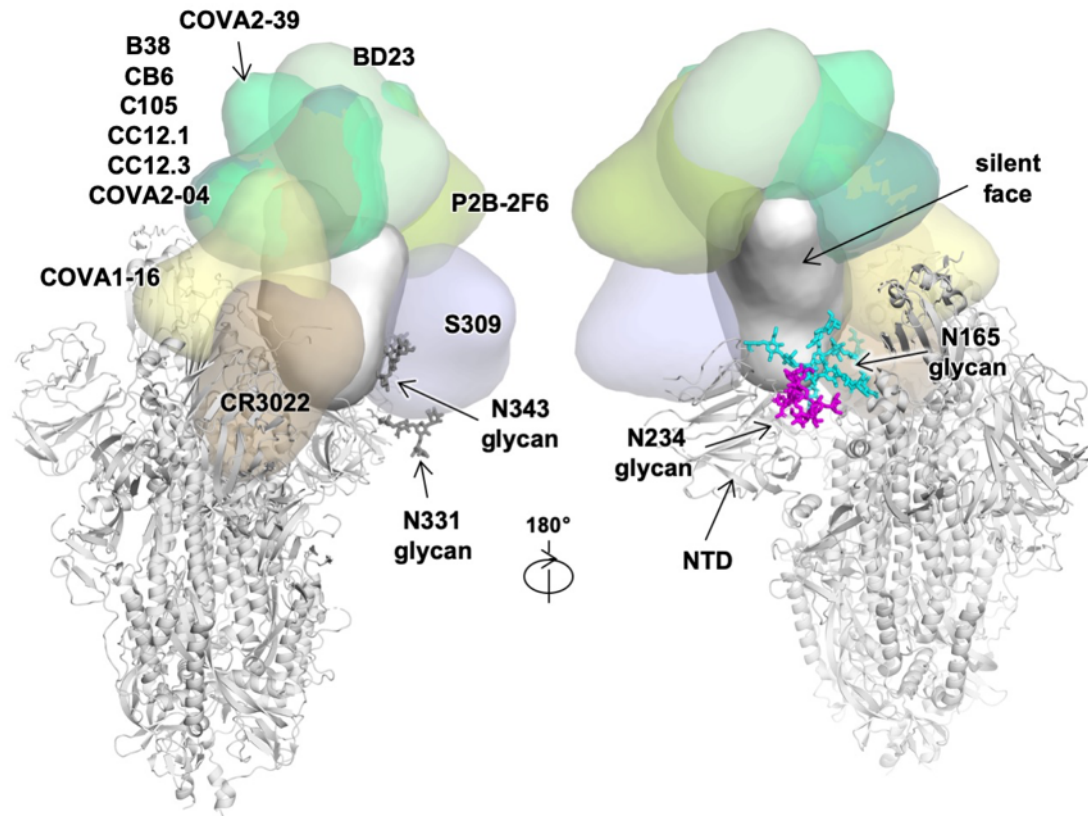
Supplementary Figure 11. The N-glycan on the N-terminal domain (NTD) also shields part of the RBD. The antibody-bound RBD, which is displayed and colored as in Figure 5, is shown in the up conformation on the S protein (PDB 6VSB) [5]. N-glycans on N165 (NTD), N234, N331, and N343 (RBD) are modelled according to the main glycoform observed at these sites in [6], and shown in stick representation. Antibody Fabs from published crystal and cryo-EM structures are represented as globular outlines in different colors as outlined in F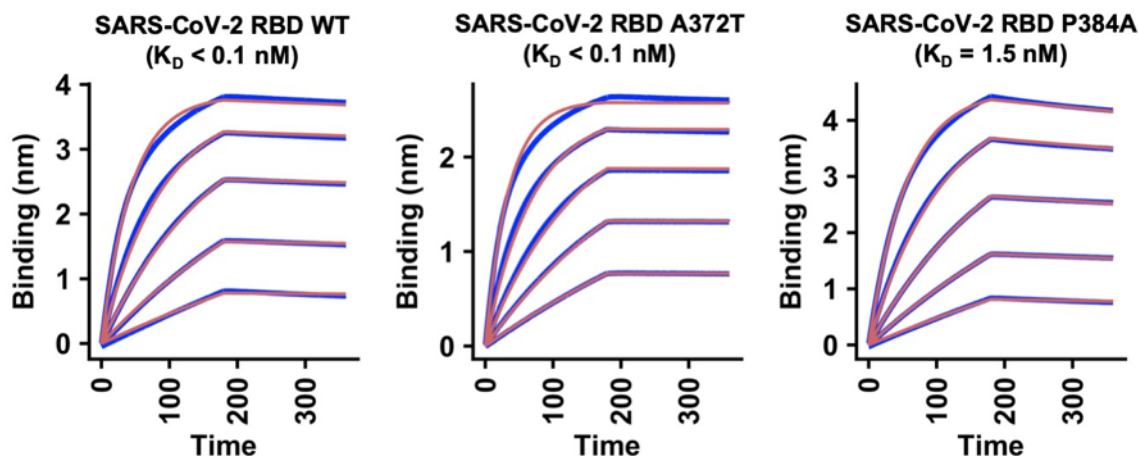igure 5. B38, CB6, C105, CC12.1, CC12.3, COVA2-04, COVA2-39, BD23, P2B-2F6 all bind at or around the receptor binding site. S309 binds to the elongated accessible face of the RBD in both up and down conformations, and CR3022 binds to the opposite face that is exposed in the RBD up conformation, but buried in the RBD down conformation.

113

114

Supplementary Figure 12. Sensorgrams for binding of COVA1-16 IgG to SARS-CoV-2 RBD WT or mutants. Binding kinetics of COVA1-16 IgG to SARS-CoV-2 RBD WT, A372T, and P384A were measured by biolayer interferometry (BLI) with RBD on the biosensor and antibody in solution. Y-axis represents the response. Dissociation constants (K_D) for Fabs were obtained using a 1:1 binding model, which are represented by the red lines. Representative results of two replicates for each experiment are shown. A372T and P384A are the only two mutations that differ between the SARS-CoV-2 and SARS-CoV sequences in COVA1-16 epitope. The affinity of COVA1-16 IgG to the A372T mutant did not show any detectable difference from WT. Although the affinity (K_D) of COVA1-16 IgG to the P384A mutant decreases, the binding is still 100 times tighter than that measured between COVA1-16 IgG and SARS-CoV RBD (Figure S4B). As a result, the binding affinity of COVA1-16 to the RBD may be influenced by residues outside of the epitope as well as the dynamics of the RBD fluctuations between up and down conformations.

15

129   **Supplementary Table 1. X-ray data collection and refinement statistics**

130

Data collection		
	COVA1-16 Fab + SARS-CoV-2 RBD	COVA1-16 Fab
Beamline	SSRL 12-1	SSRL 12-1
Wavelength (Å)	0.97946	0.97946
Space group	$P\,1\,2_1\,1$	$P\,4_1\,3\,2$
Unit cell parameters		
a, b, c (Å)	57.4, 124.9, 57.6	156.3, 156.3, 156.3
α, β, γ (°)	90, 96.1, 90	90, 90, 90
Resolution (Å) [a]	50.0-2.89 (2.95-2.89)	50.0-2.53 (2.58-2.53)
Unique reflections [a]	17,656 (845)	22,357 (1,084)
Redundancy [a]	3.7 (3.2)	37.0 (14.1)
Completeness (%) [a]	97.9 (93.9)	100.0 (100.0)
$<I/\sigma_I>$ [a]	7.4 (1.2)	21.5 (1.3)
R_{sym} [b] (%) [a]	15.3 (69.1)	23.6 (>100)
R_{pim} [b] (%) [a]	9.0 (42.9)	3.8 (54.3)
$CC_{1/2}$ [c] (%) [a]	96.3 (66.8)	99.6 (52.1)
Refinement statistics		
Resolution (Å)	42.8-2.89	34.1-2.53
Reflections (work)	17,632	21,872
Reflections (test)	948	1,069
R_{cryst} [d] / R_{free} [e] (%)	23.7/29.4	21.2/24.4
No. of atoms	4,873	3,284
Macromolecules	4,845	3,223
Glycans	28	-
Average B-values (Å^2)	49	43
Macromolecules	49	43
Fab	45	43
RBD	56	-
Glycans	89	-
Wilson B-value (Å^2)	43	40
RMSD from ideal geometry		
Bond length (Å)	0.004	0.007
Bond angle (°)	0.74	1.02
Ramachandran statistics (%) [f]		
Favored	95.9	96.7
Outliers	0.16	0.0
PDB code	pending	pending

131   [a] Numbers in parentheses refer to the highest resolution shell.

132   [b] $R_{sym} = \Sigma_{hkl}\,\Sigma_i\,|\,I_{hkl,i} - <I_{hkl}>\,|\,/\,\Sigma_{hkl}\,\Sigma_i\,I_{hkl,i}$ and $R_{pim} = \Sigma_{hkl}\,(1/(n\text{-}1))^{1/2}\,\Sigma_i\,|\,I_{hkl,i} - <I_{hkl}>\,|\,/\,\Sigma_{hkl}\,\Sigma_i\,I_{hkl,i}$, where $I_{hkl,i}$ is the scaled

133   intensity of the ith measurement of reflection h, k, l, $<I_{hkl}>$ is the average intensity for that reflection, and n is the

134   redundancy.

135   [c] $CC_{1/2}$ = Pearson correlation coefficient between two random half datasets.

136   [d] $R_{cryst} = \Sigma_{hkl}\,|\,F_o - F_c\,|\,/\,\Sigma_{hkl}\,|\,F_o\,|\,\times 100$, where F_o and F_c are the observed and calculated structure factors, respectively.

137   [e] R_{free} was calculated as for R_{cryst}, but on a test set comprising 5% of the data excluded from refinement.

138   [f] From MolProbity [7].

139

140 **Supplementary Table 2. Hydrogen bonds identified in the antibody-RBD interface**
141 **using the PISA program**
142
143

COVA1-16 Fab	Distance [Å]	SARS-CoV-2 RBD
H:ARG100b[NH2]	3.3	A:TYR369[O]
H:ARG100b[NE]	3.9	A:SER371[O]
H:ARG100b[N]	3.8	A:PHE377[O]
H:TYR100[N]	2.6	A:CYS379[O]
H:GLN101[NE2]	3.1	A:GLN414[OE1]
H:ARG97[NH1]	2.5	A:ASP427[O]
H:TYR32[OH]	3.1	A:ASP427[OD1]
H:THR28[N]	3.2	A:ASP427[OD2]
H:ARG97[NH1]	3.0	A:PHE429[O]
H:TYR100[O]	2.9	A:CYS379[N]
H:SER100c[O]	3.3	A:THR385[OG1]
H:GLN101[OE1]	3.8	A:GLN414[NE2]
L:ASN53[OD1]	3.2	A:ARG408[NH2]
L:LEU54[O]	3.7	A:ARG408[NE]

SUPPLEMENTARY REFERENCES

1. Huo J, Zhao Y, Ren J, Zhou D, Duyvesteyn HME, Ginn HM, et al. Neutralization of SARS-CoV-2 by destruction of the prefusion spike. Cell Host Microbe. 2020. Epub 2020/06/26. doi: 10.1016/j.chom.2020.06.010. PubMed PMID: 32585135; PubMed Central PMCID: PMCPMC7303615.

2. Pinto D, Park YJ, Beltramello M, Walls AC, Tortorici MA, Bianchi S, et al. Cross-neutralization of SARS-CoV-2 by a human monoclonal SARS-CoV antibody. Nature. 2020. Epub 2020/05/19. doi: 10.1038/s41586-020-2349-y. PubMed PMID: 32422645.

3. Walls AC, Park YJ, Tortorici MA, Wall A, McGuire AT, Veesler D. Structure, function, and antigenicity of the SARS-CoV-2 spike glycoprotein. Cell. 2020;181:281-92.e6. Epub 2020/03/11. doi: 10.1016/j.cell.2020.02.058. PubMed PMID: 32155444.

4. Lawrence MC, Colman PM. Shape complementarity at protein/protein interfaces. J Mol Biol. 1993;234(4):946-50. Epub 1993/12/20. doi: 10.1006/jmbi.1993.1648. PubMed PMID: 8263940.

5. Wrapp D, Wang N, Corbett KS, Goldsmith JA, Hsieh CL, Abiona O, et al. Cryo-EM structure of the 2019-nCoV spike in the prefusion conformation. Science. 2020;367:1260-3. Epub 2020/02/23. doi: 10.1126/science.abb2507. PubMed PMID: 32075877.

6. Watanabe Y, Allen JD, Wrapp D, McLellan JS, Crispin M. Site-specific glycan analysis of the SARS-CoV-2 spike. Science. 2020;369:330-3. Epub 2020/05/06. doi: 10.1126/science.abb9983. PubMed PMID: 32366695; PubMed Central PMCID: PMCPMC7199903.

7. Chen VB, Arendall WB, 3rd, Headd JJ, Keedy DA, Immormino RM, Kapral GJ, et al. MolProbity: all-atom structure validation for macromolecular crystallography. Acta Crystallogr D Biol Crystallogr. 2010;66(Pt 1):12-21. doi: 10.1107/S0907444909042073. PubMed PMID: 20057044; PubMed Central PMCID: PMCPMC2803126.